



# An Introduction to Seismology, Earthquakes, and Earth Structure

Seth Stein

*Department of Geological Sciences, Northwestern University, Evanston, Illinois*

Michael Wysession

*Department of Earth and Planetary Sciences, Washington University, St Louis, Missouri*

*QE534*  
*.S74*  
*2000*

© by 2003 by S. Stein and M. Wysession

350 Main Street, Malden, MA 02148-5020, USA  
108 Cowley Road, Oxford OX4 1JF, UK  
550 Swanston Street, Carlton, Victoria 3053, Australia

The right of the Authors to be identified as the Authors of this Work has been asserted in accordance with the UK Copyright, Designs, and Patents Act 1988.

All rights reserved. No part of this publication may be reproduced, stored in a retrieval system, or transmitted, in any form or by any means, electronic, mechanical, photocopying, recording or otherwise, except as permitted by the UK Copyright, Designs, and Patents Act 1988, without the prior permission of the publisher.

First published 2003 by Blackwell Publishing Ltd.  
Reprinted 2003

*Library of Congress Cataloging-in-Publication Data*

Stein, Seth.

An introduction to seismology, earthquakes, and earth structure /  
Seth Stein, Michael Wysession.

p.cm.

Includes bibliographical references and index.

ISBN 0-86542-078-5 (pb. : alk. paper)

1. Seismology. 2. Geology, Structural. 3. Earthquakes.

I. Wysession, Michael. II. Title.

QE534.3 .S74 2002  
551.22 —dc21 2001052639

A catalogue record for this title is available from the British Library.

Set in 9.5 on 11 pt Sabon  
by Graphicraft Ltd, Hong Kong  
Printed and bound in the UK  
by TJ International Ltd, Padstow, Cornwall

For further information on  
Blackwell Publishing, visit our website:  
<http://www.blackwellpublishing.com>

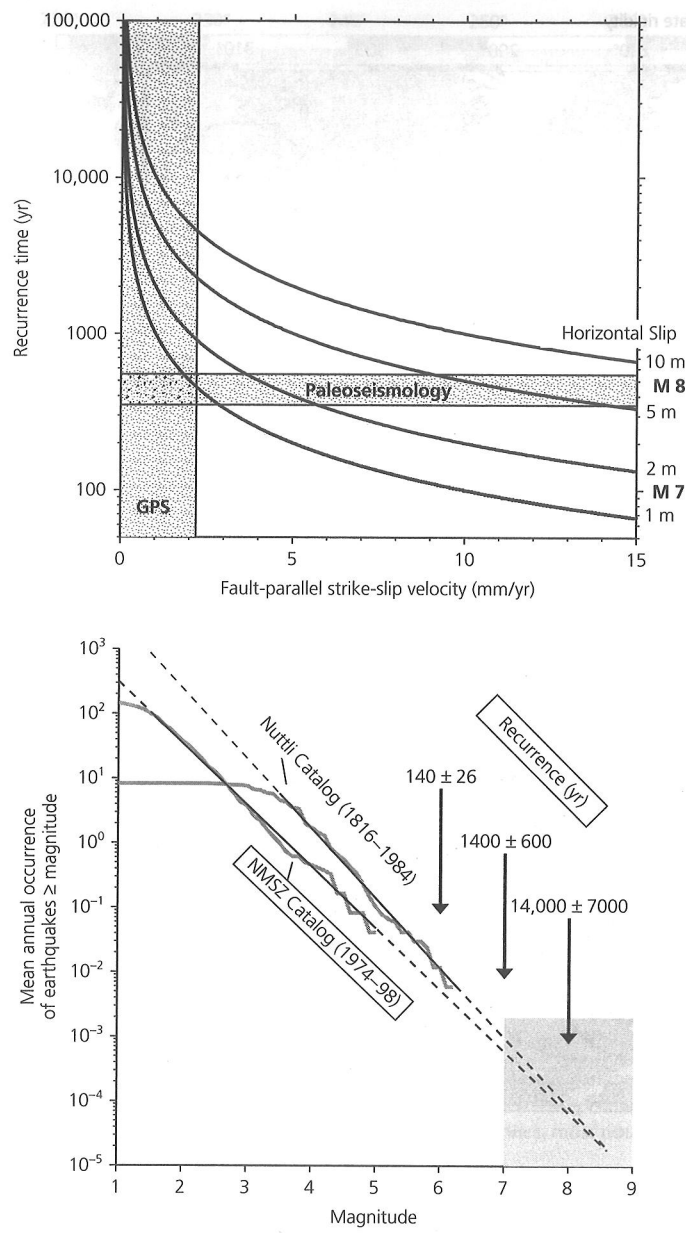


Fig. 5.6-16 Top: Relation between interseismic motion and the expected recurrence of large New Madrid earthquakes. The recurrence estimates from paleoseismic studies and geodetic data are jointly consistent with slip in the 1811–12 earthquakes of about 1 m, corresponding to a low-magnitude 7 earthquake. Bottom: Earthquake frequency–magnitude data for the New Madrid zone. Both the instrumental and historic (1816–1984) data predict a recurrence interval of about 1000 yr for magnitude 7 earthquakes. (Newman *et al.*, 1999. *Science*, 284, 619–21, copyright 1999 American Association for the Advancement of Science.)

margins, even those that have not been recently deglaciated. Stresses associated with the removal of glacial loads may also play a role in causing earthquakes within continental interiors such as the northeastern USA and eastern Canada. It has also been suggested that the huge 1998 Balleny Island intraplate

earthquake (Section 5.5.1) may have been triggered by stresses due to the shrinking Antarctic ice cap.

As in the oceans, another interesting class of intraplate seismicity is associated with hot spots. The area near the Yellowstone hot spot in the western USA shows an intriguing pattern of seismicity along the margins of the Snake River plain (Fig. 5.6-21), which is the volcanic track the hot spot produced as the North American plate moved over it (Fig. 5.2-8). This seismicity, which includes the 1959  $M_s$  7.5 Hebgen Lake, Montana,<sup>6</sup> and 1983  $M_s$  7.3 Borah Peak, Idaho, earthquakes, forms a parabolic pattern extending southwestward from Yellowstone itself. It thus stands out from the regional seismicity (Fig. 5.2-3) associated with the extensional tectonics of the eastern portion of the Basin and Range province, termed the Intermountain Seismic Belt. The absence of seismicity along the track itself seems likely to be a consequence of the thermal and magmatic perturbations produced by the hot spot, although the specific mechanism is still under discussion. Seismic tomography (Fig. 5.6-21) shows a low-velocity anomaly in the crust and upper mantle under Yellowstone itself, presumably due to partial melting and hydrothermal fluids, and a deeper anomaly that persists along the track.

In summary, although continental intraplate seismicity is a minor fraction of global seismic moment release, it has both scientific and societal interest precisely because it is rare. It provides one of our few ways of studying the limits of plate rigidity and intraplate stresses, and poses the challenge of deciding the appropriate level of earthquake preparedness for rare, but potentially destructive, earthquakes.

## 5.7 Faulting and deformation in the earth

Because earthquake faulting is a spectacular manifestation of the processes that deform the solid earth, we seek to understand how earthquakes result from and reflect this deformation. Valuable insight comes from laboratory experiments and theoretical models for the behavior of solid materials. Although the experiments and models are much simpler than the complexities of the real earth, they allow us to think about key features. Seismology and geophysics thus exploit research devoted to material behavior by a range of disciplines, including engineering, materials science, and solid state physics. We touch only briefly on some basic ideas, and more information can be found in the references at the end of the chapter.

### 5.7.1 Rheology

Materials can be characterized by their *rheology*, the way they deform. In seismology we typically take a continuum

<sup>6</sup> This earthquake triggered an enormous landslide that buried a campground, causing 28 deaths and dammed the Madison River, forming Quake Lake. These dramatic effects are still visible today and make the site well worth visiting. A visitor center and parking lot are built on the slide.

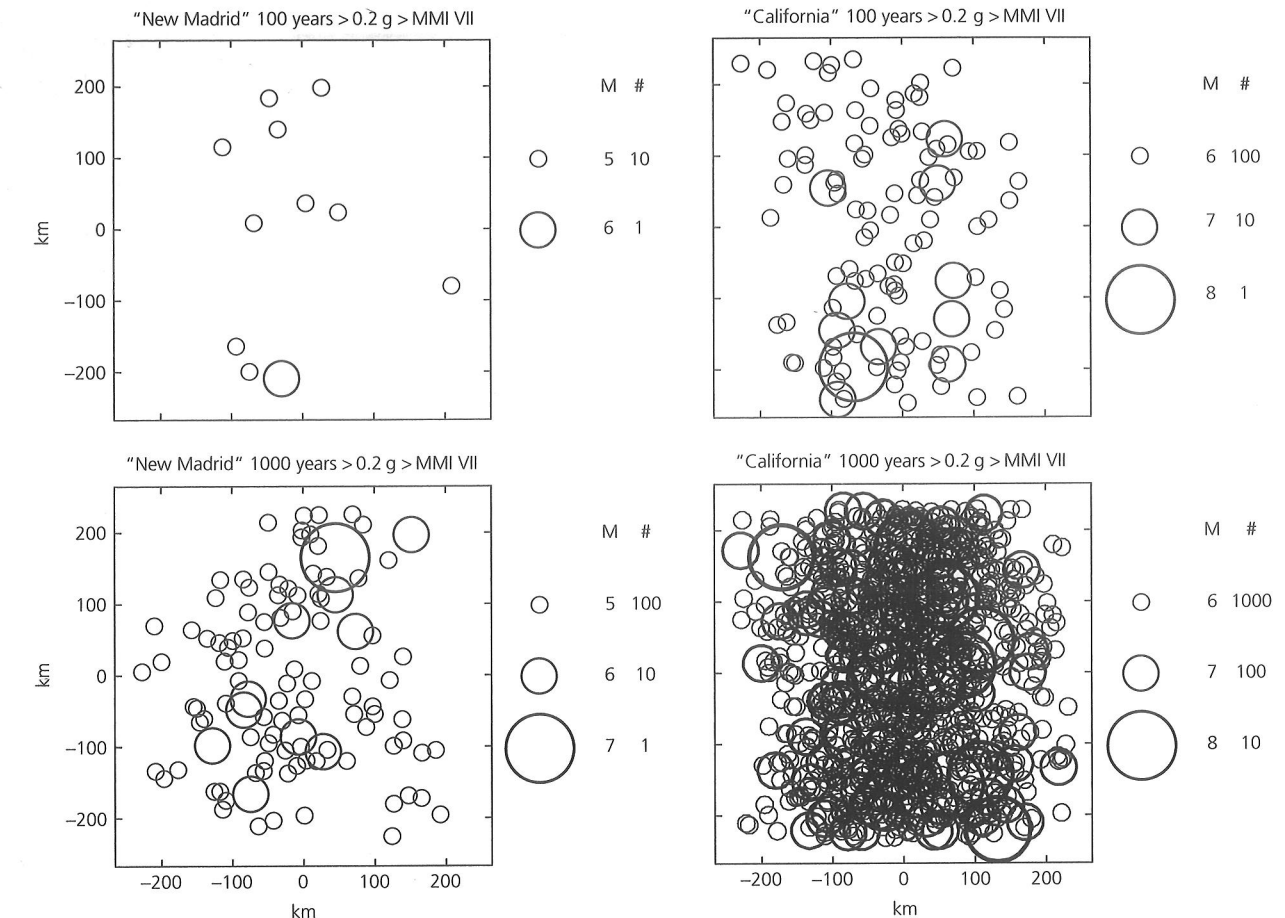


Fig. 5.6-17 Schematic illustration of the relation between the recurrence times of seismicity and resulting seismic hazard for the intraplate New Madrid seismic zone and the southern California plate boundary zone. Seismicity is assumed to be randomly distributed about an N–S line through 0, with California 100 times more active, but New Madrid earthquakes causing potentially serious damage (circles show areas with acceleration 0.2 g or greater, Table 1.2-4) over an area comparable to that for a California earthquake one magnitude unit larger.

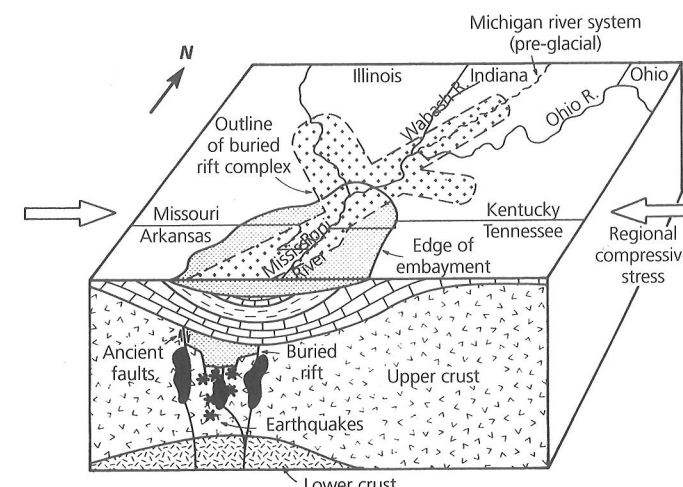


Fig. 5.6-18 Schematic tectonic model for the New Madrid earthquakes. (Braile *et al.*, 1986. *Tectonophysics*, 131, 1–21, with permission from Elsevier Science.)

approach, considering the earth to be a continuous deformable material. This means that we focus on its aggregate behavior (Section 2.3) rather than on how its behavior is determined by what happens at a microscopic scale.

To do this, consider the strain that results from compressing a rock specimen. The simplest case is shown in Fig. 5.7-1a. For small stresses, the resulting strain is proportional to the applied stress, so the material is purely *elastic*. Elastic behavior happens when seismic waves pass through rock, because the strains are small (Section 2.3.8). However, once the applied stress reaches a value  $\sigma_f$ , known as the rock's *fracture strength*, the rock suddenly breaks. Such *brittle* fracture is the simplest model for what happens when an earthquake occurs on a fault. Thus brittle fracture — a deviation from elasticity — generates elastic seismic waves.

Other materials show a change in the stress-strain curve for increasing stresses (Fig. 5.7-1b). For stresses less than the *yield stress*,  $\sigma_y$ , the material acts elastically. Thus, if the stress is released, the strain returns to zero. However, for stresses greater

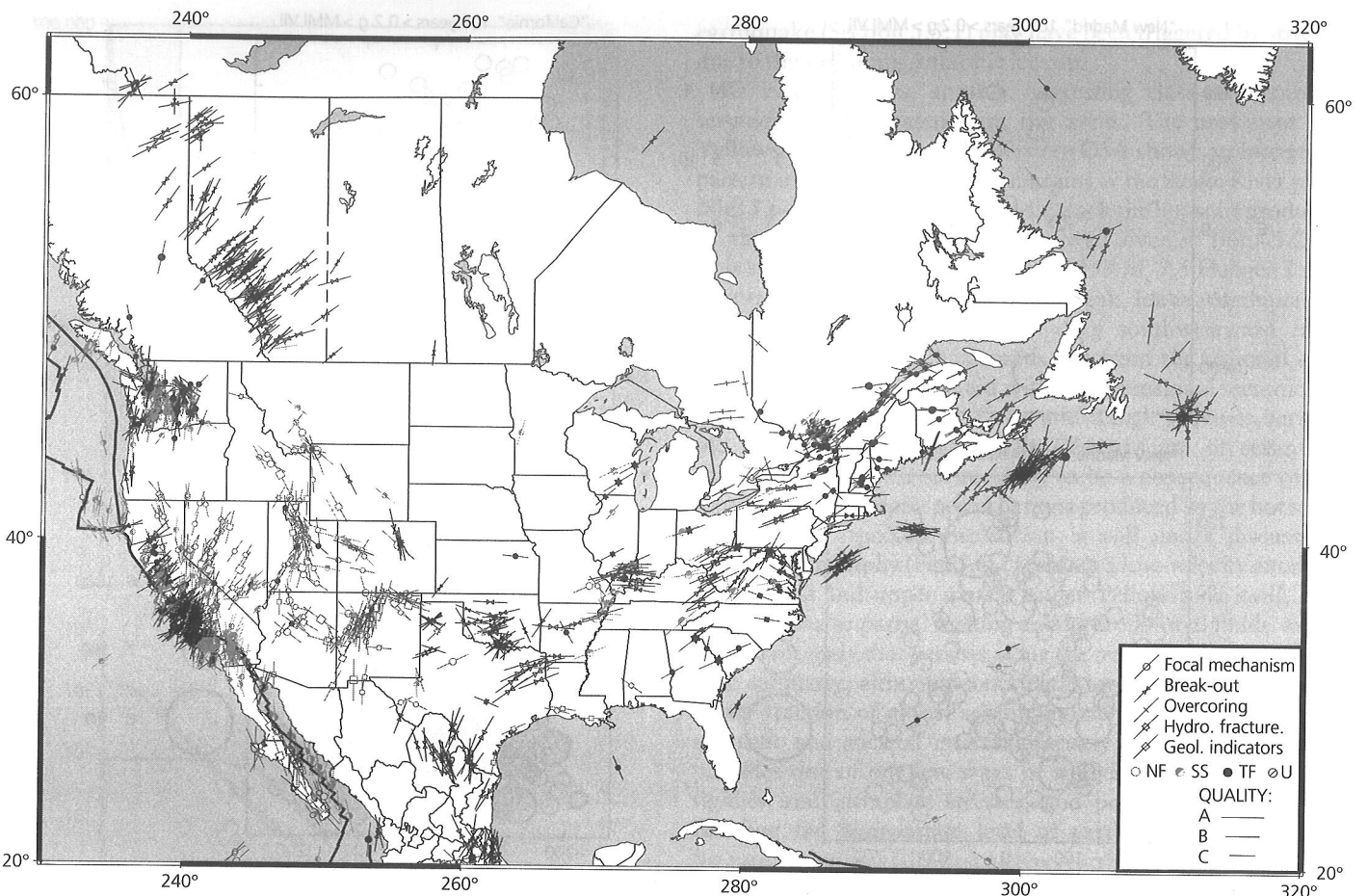


Fig. 5.6-19 Stress map for North America. (World Stress Map project, 2000. Courtesy of the US Geological Survey.)

than the yield stress, releasing the stress relieves the elastic portion of the strain, but leaves a permanent deformation (Fig. 5.7-1c). If the material is restressed, the stress-strain curve now includes the point of the permanent strain. The material behaves as though its elastic properties were unchanged, but the yield strength has increased from  $\sigma_0$  to  $\sigma'_0$ . The portion of the stress-strain curve corresponding to stress above the yield stress is called *plastic* deformation, in contrast to the elastic region where no permanent deformation occurs. Materials showing significant plasticity are called *ductile*. A common approximation is to treat ductile materials as *elastic-perfectly plastic*: stress is proportional to strain below the yield stress and constant for all strains when stress exceeds the yield stress (Fig. 5.7-2).

An important result of laboratory experiments is that at low pressures rocks are brittle, but at high pressures they behave ductilely, or flow. Figure 5.7-3 shows experiments where a rock is subjected to a compressive stress  $\sigma_1$  that exceeds a confining pressure  $\sigma_3$ . For confining pressures less than about 400 MPa the material behaves brittlely — it reaches the yield strength, then fails. For higher confining pressures the material

flows ductilely. These pressures occur not far below the earth's surface — as discussed earlier, 3 km depth corresponds to 100 MPa pressure — so 800 MPa is reached at about 24 km. This experimental result is consistent with the idea that the strong lithosphere is underlain by the weaker asthenosphere.

A related phenomenon is that materials behave differently at different time scales. A familiar example is that although an asphalt driveway is solid if one falls on it, a car parked on it during a hot day can sink a little ways into it. On short time scales the driveway acts rigidly, but on longer time scales it starts to flow as a *viscous fluid*. This effect is crucial in the earth, because the mantle is solid on the time scale needed for seismic waves to pass through it, but flows on geological time scales.

### 5.7.2 Rock fracture and friction

The first question we address is how and when rocks break. In the brittle regime of behavior, the development of faults and the initiation of sliding on preexisting faults depend on the applied stresses.

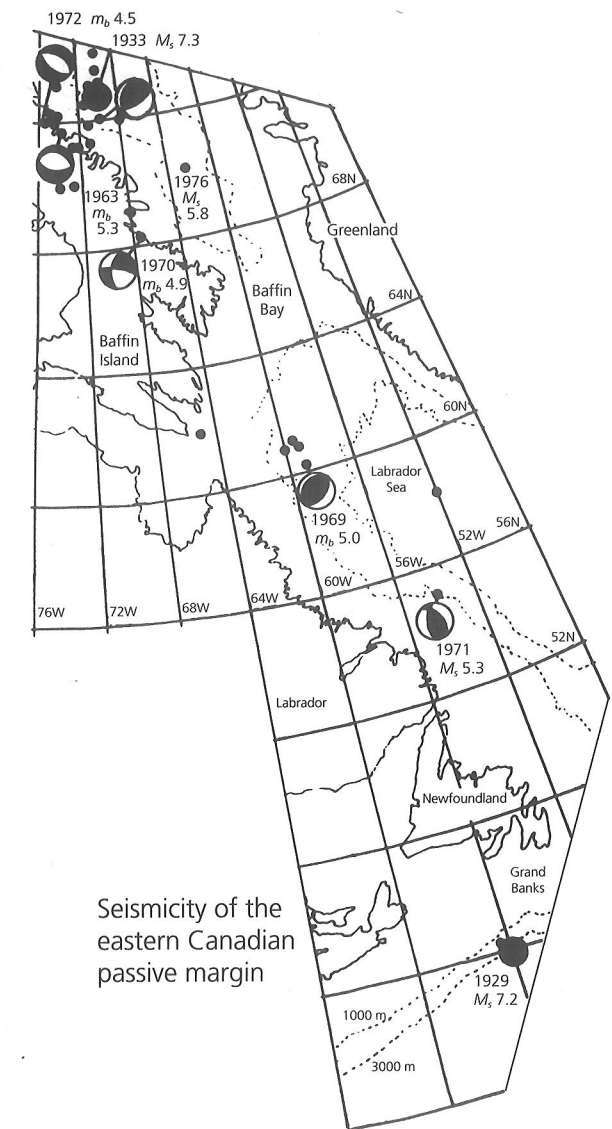


Fig. 5.6-20 Earthquakes along the passive continental margin of eastern Canada. These earthquakes may have occurred on faults remaining from continental rifting. (Stein *et al.*, 1979. *Geophys. Res. Lett.*, 6, 537–40, copyright by the American Geophysical Union.)

Given a stress field specified by a stress tensor, we use the approach of Section 2.3.3 to find the variation in normal and shear stress on faults of various orientations. For simplicity, we consider the stress in two dimensions. If the coordinate axes ( $\hat{e}_1, \hat{e}_2$ ) are oriented in the principal stress directions, the stress tensor is diagonal,

$$\sigma_{ij} = \begin{pmatrix} \sigma_1 & 0 \\ 0 & \sigma_2 \end{pmatrix}. \quad (1)$$

To find the stress on a plane whose normal  $\hat{e}'_1$  is at an angle of  $\theta$  from  $\hat{e}_1$ , the direction of  $\sigma_1$  (Fig. 5.7-4), we transform the stress

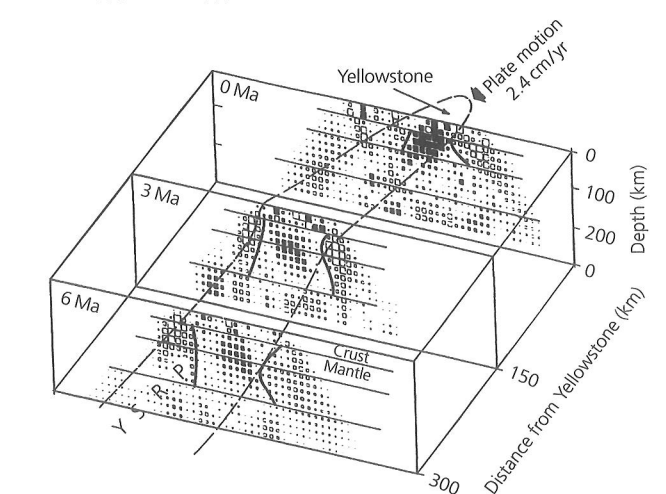
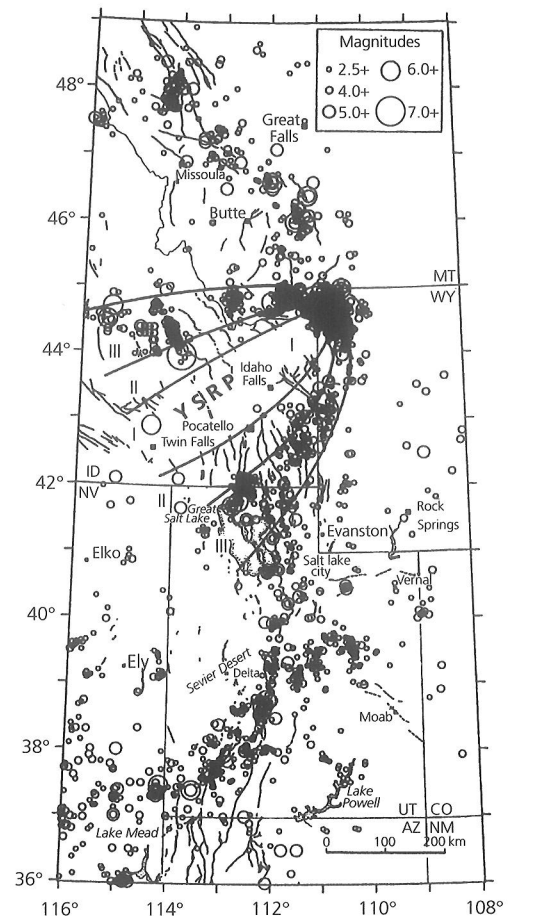


Fig. 5.6-21 Top: Seismicity (1900–85) of the Intermountain area of the western USA. Superimposed on the regional seismicity are earthquakes forming a parabola along the margins of the Yellowstone–Snake River plain (YRSP), the volcanic track of the Yellowstone hot spot. Bottom: P-wave velocities across the hot spot track, shown by squares scaled in size to the differences from a uniform-velocity model. The largest symbols are ±3%, with dark and open symbols showing low and high velocities. (Smith and Braile, 1994. *J. Volcan. Geotherm. Res.*, 61, 121–87, with permission from Elsevier Science.)

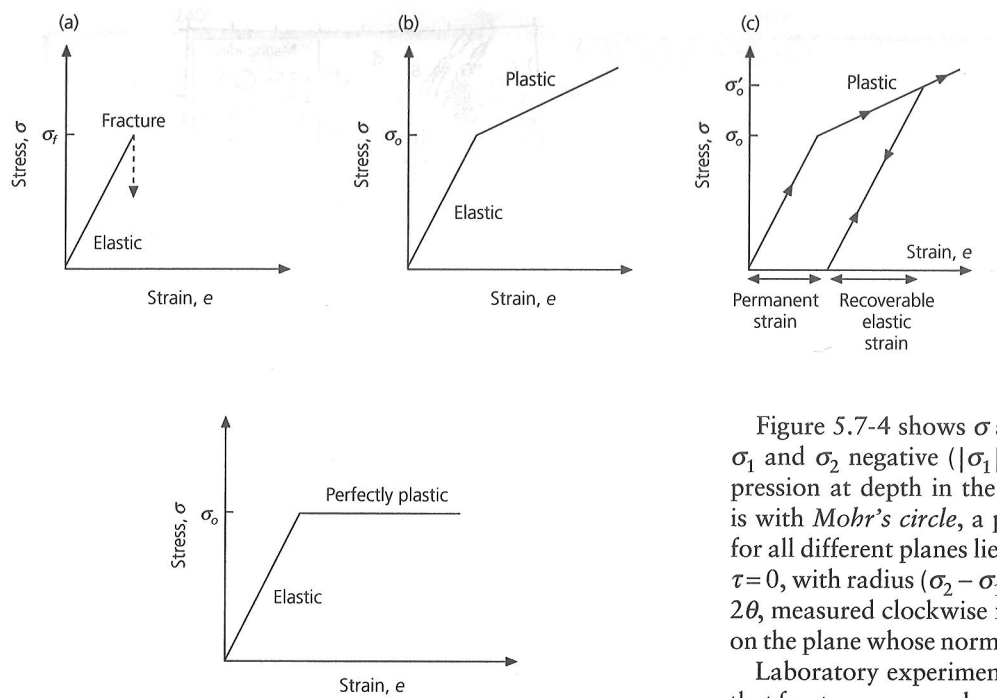


Fig. 5.7-1 (a): A material is perfectly elastic until it fractures when the applied stress reaches  $\sigma_f$ . (b): A material undergoes plastic deformation when the stress exceeds a yield stress  $\sigma_o$ . (c): A permanent strain results from plastic deformation when the stress is raised to  $\sigma'_o$  and released.

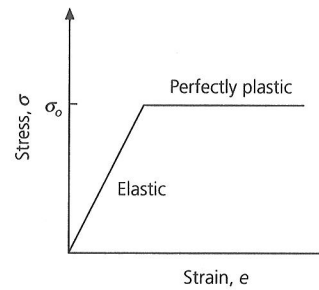


Fig. 5.7-2 An elastic–perfectly plastic rheology, which is a commonly used approximation for the behavior of ductile materials.

tensor from the principal axis coordinate system to a new coordinate system using the transformation matrix (Section 2.3.3)

$$A = \begin{pmatrix} \cos \theta & \sin \theta \\ -\sin \theta & \cos \theta \end{pmatrix} \quad (2)$$

so that the stress in the new (primed) system is

$$\begin{aligned} \sigma'_{ij} &= A\sigma A^T = \begin{pmatrix} \cos \theta & \sin \theta \\ -\sin \theta & \cos \theta \end{pmatrix} \begin{pmatrix} \sigma_1 & 0 \\ 0 & \sigma_2 \end{pmatrix} \begin{pmatrix} \cos \theta & -\sin \theta \\ \sin \theta & \cos \theta \end{pmatrix} \\ &= \begin{pmatrix} \sigma_1 \cos^2 \theta + \sigma_2 \sin^2 \theta & (\sigma_2 - \sigma_1) \sin \theta \cos \theta \\ (\sigma_2 - \sigma_1) \sin \theta \cos \theta & \sigma_1 \sin^2 \theta + \sigma_2 \cos^2 \theta \end{pmatrix}. \end{aligned} \quad (3)$$

The normal and shear stresses on the plane vary, depending on the plane's orientation. The normal stress component, denoted by  $\sigma$ , is

$$\sigma = \sigma'_{11} = \sigma_1 \cos^2 \theta + \sigma_2 \sin^2 \theta = \frac{(\sigma_1 + \sigma_2)}{2} + \frac{(\sigma_1 - \sigma_2)}{2} \cos 2\theta, \quad (4a)$$

and the shear component, denoted by  $\tau$ , is

$$\tau = \sigma'_{12} = (\sigma_2 - \sigma_1) \sin \theta \cos \theta = \frac{(\sigma_2 - \sigma_1)}{2} \sin 2\theta. \quad (4b)$$

Figure 5.7-4 shows  $\sigma$  and  $\tau$  as functions of  $\theta$  for the case of  $\sigma_1$  and  $\sigma_2$  negative ( $|\sigma_1| > |\sigma_2|$ ), which corresponds to compression at depth in the earth. A graphic way to show these is with *Mohr's circle*, a plot of  $\sigma$  versus  $\tau$  (Fig. 5.7-5). Values for all different planes lie on a circle centered at  $\sigma = (\sigma_1 + \sigma_2)/2$ ,  $\tau = 0$ , with radius  $(\sigma_2 - \sigma_1)/2$ . The point on the circle with angle  $2\theta$ , measured clockwise from the  $-\sigma$  axis, gives the  $\sigma$ ,  $\tau$  values on the plane whose normal is at angle  $\theta$  to  $\sigma_1$ .<sup>1</sup>

Laboratory experiments on rocks under compression show that fracture occurs when a critical combination of the absolute value of shear stress and the normal stress is exceeded. This relation, known as the *Coulomb–Mohr failure criterion*, can be stated as

$$|\tau| = \tau_o - n\sigma, \quad (5)$$

where  $\tau_o$  and  $n$  are properties of the material known as the *cohesive strength* and *coefficient of internal friction*. (The minus sign reflects the convention that compressional stresses are negative.) The failure criterion plots as two lines in the  $\tau$ - $\sigma$  plane, with  $\tau$  axis intercepts  $\pm \tau_o$  and slope  $\pm n$  (Fig. 5.7-6). If the principal stresses are  $\sigma_1$ ,  $\sigma_2$ , such that Mohr's circle does not intersect the failure lines, the material does not fracture. However, given the same  $\sigma_2$  but a higher  $\sigma'_1$ , Mohr's circle intersects the line, and the material breaks.

The failure lines show how much shear stress,  $\tau$ , can be applied to a surface subject to a normal stress  $\sigma$  before failure occurs. The cohesive strength is the minimum (absolute value) shear stress for failure. The coefficient of internal friction indicates the additional shear stress sustainable as the normal stress increases. Thus, deeper in the crust, where the pressure and hence normal stress are higher, rocks are stronger, and higher shear stress is required to break them.

The failure lines and Mohr's circle show on which plane failure occurs for a given stress state. To find  $\theta$ , the angle between the plane's normal and the maximum compressive stress ( $\sigma_1$ ) direction, we write the failure lines as

$$|\tau| = \tau_o - \sigma \tan \phi, \quad (6)$$

<sup>1</sup> Following the seismological convention of compressive stresses being negative, Mohr's circle is shown for  $\sigma < 0$ . The opposite convention is often used in rock mechanics, e.g. Figs. 5.7-3 and 5.7-10.

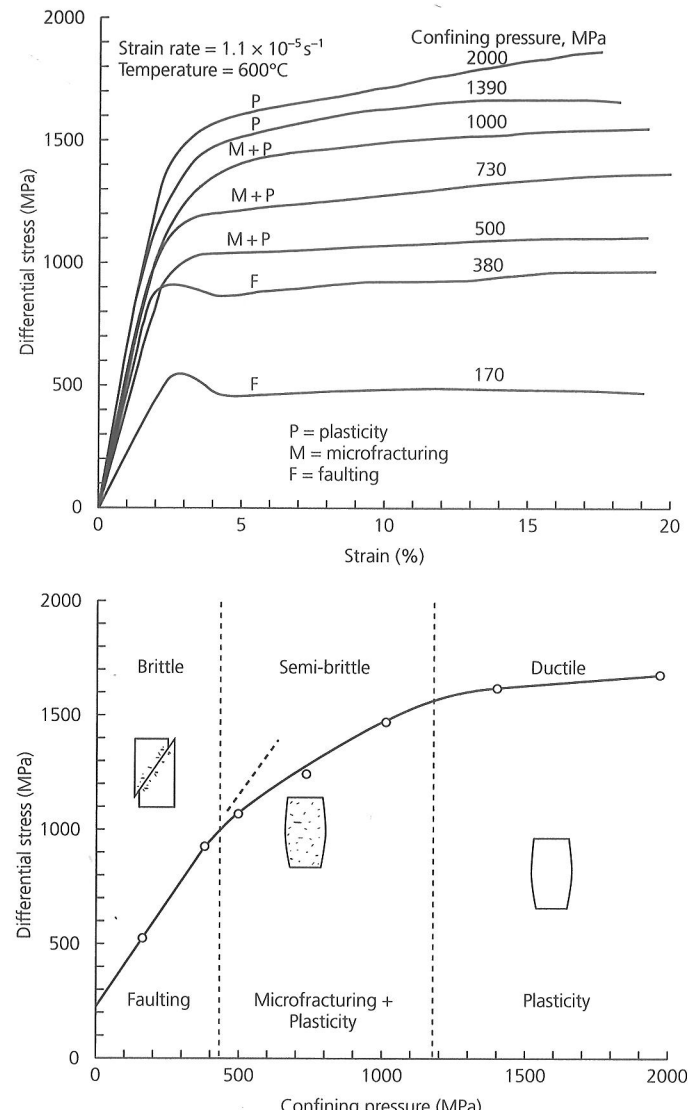


Fig. 5.7-3 Results of an experiment in which rocks are subjected to a compressive stress  $\sigma_1$  greater than the confining pressure  $\sigma_3$ . Top: Differential stress ( $\sigma_1 - \sigma_3$ ) versus strain (compare to Figs. 5.7-1 and 2) curves for various confining pressures. Bottom: Ultimate strength ( $\sigma_1 - \sigma_3$  at 10% strain rate, from top) for various confining pressures. For low (< 400 MPa) confining pressures, the material fractures, and its strength increases with pressure. For higher pressures, the material is ductile, and its strength increases only slowly with pressure. A semi-brittle transition regime, in which both microfractures and crystal plasticity occur, separates the brittle and ductile regimes. (Kirby, 1980. *J. Geophys. Res.*, 85, 6353–63, copyright by the American Geophysical Union.)

where  $n = \tan \phi$ , and  $\phi$ , the *angle of internal friction*, is formed by extending the failure line to the  $\sigma$  axis (Fig. 5.7-7). Fracture occurs at point F, where the failure line is tangent to Mohr's circle. Considering the right triangle AFB, we see that

$$\phi = 2\theta - 90^\circ, \text{ so } \theta = \phi/2 + 45^\circ. \quad (7)$$

For example, in introducing the relation between fault plane solutions and crustal stresses in Section 2.3.5, we made the simplest assumption that fracture occurs at  $45^\circ$  to the principal stress axes, corresponding to the case  $\phi = 0^\circ$ ,  $n = 0$ ,  $\theta = 45^\circ$ . Physically, this means that the normal stress has no effect on the strength of the rock. However, rocks typically have  $n$  about 1, so  $\phi = 45^\circ$ ,  $\theta = 67.5^\circ$ , and the fault plane is closer ( $22.5^\circ$ ) to the maximum compression ( $\sigma_1$ ) direction (Fig. 5.7-8). This idea is important when using P and T axes of focal mechanisms to characterize stress directions.

Figure 5.7-7 also shows how to find the stresses when fracture occurs. Consider the point T on the failure line such that  $T\sigma_2$  is perpendicular to the  $\sigma$  axis. Because the angle  $AT\sigma_2$  is  $\theta$  (triangles AFT and A $\sigma_2$ T are congruent),

$$\overline{T\sigma_2} = A\sigma_2 \cot \theta, \quad (8)$$

or, since  $\overline{A\sigma_2} = (\sigma_2 - \sigma_1)/2$ ,

$$\overline{T\sigma_2} = \frac{(\sigma_2 - \sigma_1)}{2} \cot \theta. \quad (9)$$

Similarly,

$$\overline{T\sigma_2} = \tau_o - \sigma_2 \tan \phi \quad (10)$$

(the minus sign is because  $\sigma_2$  is negative), so

$$\frac{(\sigma_2 - \sigma_1)}{2} \cot \theta = \tau_o - \sigma_2 \tan \phi. \quad (11)$$

This relation can be written in terms of the angle of the fracture plane, using Eqn 7 and trigonometric identities,

$$\tan \phi = -\cot 2\theta = \frac{-1}{\tan 2\theta} = \frac{\tan^2 \theta - 1}{2 \tan \theta}, \quad (12)$$

yielding

$$\sigma_1 = -2\tau_o \tan \theta + \sigma_2 \tan^2 \theta. \quad (13)$$

We will use this relation between the stresses when fracture occurs to estimate the maximum stresses in the crust.

Similar analyses show when the shear stress is high enough to overcome friction and cause sliding on a previously existing fault. The results are similar to those for a new fracture in unbroken rock, except that at low stress levels the preexisting fault has no cohesive strength. Thus slip on the fault occurs when  $|\tau| = -\mu\sigma$ , where  $\mu$  is the *coefficient of sliding friction*, which can be expressed by an *angle of sliding friction*

$$\tan \alpha = \mu. \quad (14)$$

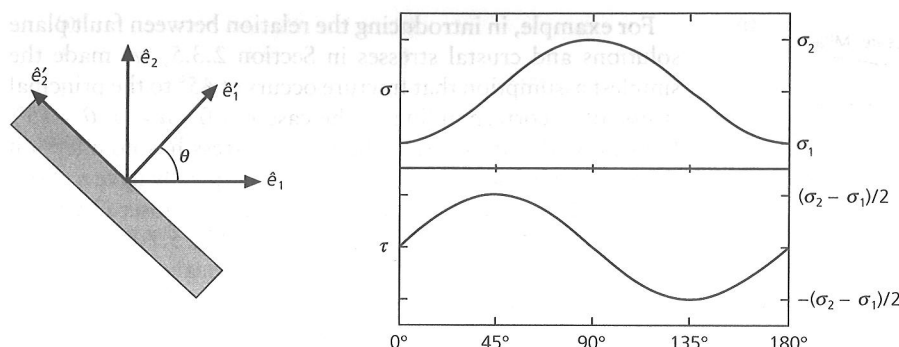


Fig. 5.7-4 Left: Geometry of a plane with normal  $\hat{e}'_1$ , oriented at an angle  $\theta$  from  $\hat{e}_1$ , the direction of the maximum compressive stress  $\sigma_1$ . Right: Normal stress,  $\sigma$ , and shear stress,  $\tau$ , as functions of the angle  $\theta$ .

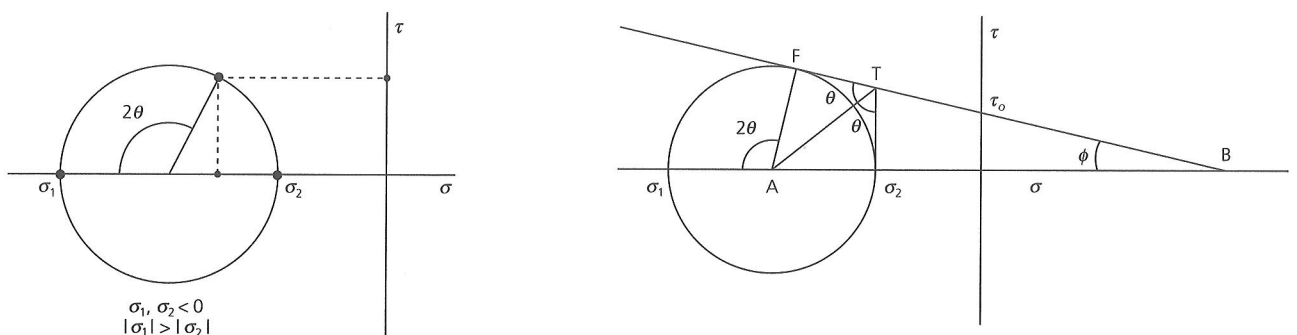


Fig. 5.7-5 Mohr's circle: Given a state of stress described by principal stresses  $\sigma_1$  and  $\sigma_2$ , the normal stress,  $\sigma$ , and the shear stress,  $\tau$ , for planes of all orientations lie on a circle with radius  $(\sigma_2 - \sigma_1)/2$ . The point on the circle with angle  $2\theta$ , measured clockwise from the  $-\sigma$  axis, gives  $\sigma$  and  $\tau$  on a plane whose normal is at an angle  $\theta$  from the direction of  $\sigma_1$ .

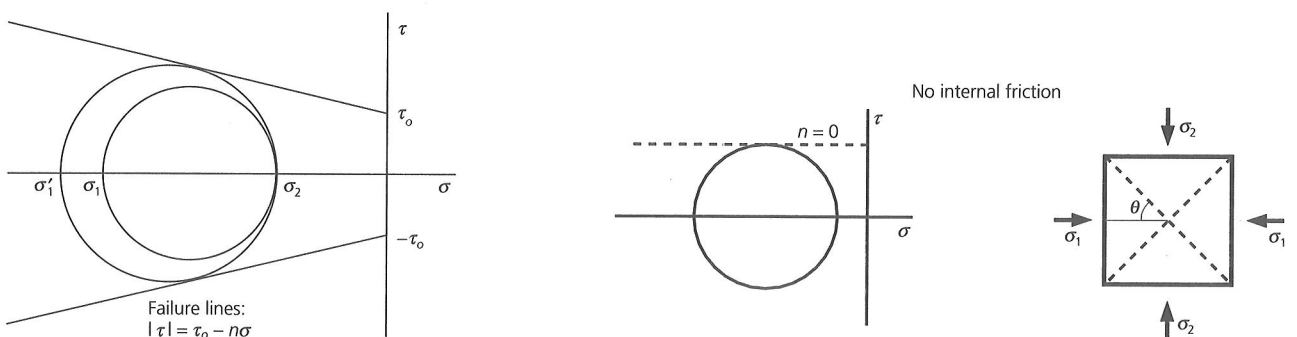


Fig. 5.7-6 The Coulomb-Mohr failure criterion assumes that a material fractures when Mohr's circle intersects the failure line.

Figure 5.7-9 shows the Mohr's circle representation of a rock with preexisting faults. In addition to the failure line, there is a frictional sliding line corresponding to

$$\tau = -\mu\sigma = -\sigma \tan \alpha \quad (15)$$

Because the sliding line starts at the origin, it is initially below the failure line. Assume that the stresses are large enough that Mohr's circle touches the failure line at the point yielding frac-

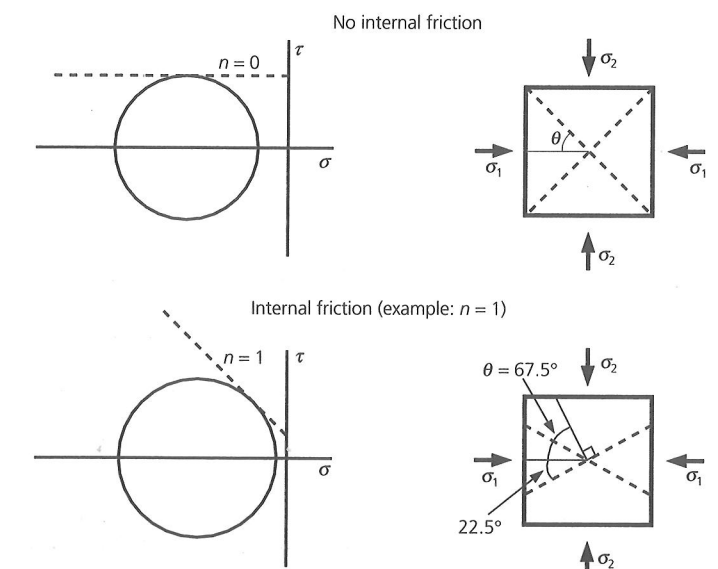


Fig. 5.7-8 With no internal friction, fracture occurs at an angle of 45°. For  $n=1$ , the fracture angle is 67.5°, and the fault plane is closer (22.5°) to the maximum compression ( $\sigma_1$ ) direction.

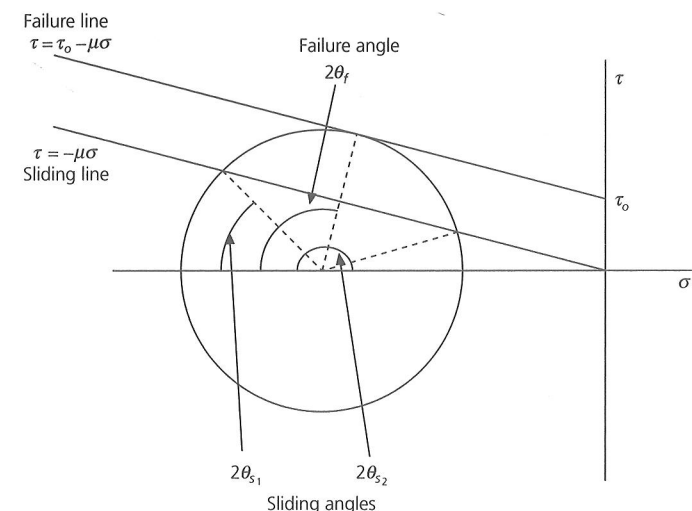


Fig. 5.7-9 Mohr's circle for sliding on a rock's preexisting faults. A new fracture would form at an angle  $\theta_f$ , given by the failure line. However, slip will occur on a preexisting fault if there are any with angles between  $\theta_{s1}$  and  $\theta_{s2}$ , given by the intersection of the circle with the frictional sliding line.

ture on a plane corresponding to an angle  $\theta_f$ . Similarly, the frictional sliding line intercepts the circle at two points, corresponding to angles  $\theta_{s1}$  and  $\theta_{s2}$ . Thus the rock can fail in several ways. If there are preexisting faults with angles  $\theta_{s1}$  or  $\theta_{s2}$ , slip on these faults may occur. Alternatively, a new fracture may form on the plane given by  $\theta_f$ . However, because this fracture occurs at higher shear stress than is needed for frictional sliding on the preexisting faults, sliding is favored over the formation of a new fracture. Thus, if the stress has gradually risen to this level, sliding on preexisting faults would probably have prevented a new fracture from forming.

This effect can have seismological consequences. The simplest way to use focal mechanisms to infer stress orientations is to assume that the earthquakes occurred on newly formed faults. However, if the rock had been initially faulted, the earthquakes may have occurred on preexisting faults. In the representation of Fig. 5.7-9, if faults exist with normals oriented between  $\theta_{s1}$  and  $\theta_{s2}$  to the maximum compressive stress, slip on these faults will occur rather than the formation of a new fracture. Thus the inferred stress direction will be somewhat inaccurate. For example, the thrust focal mechanisms along the Himalayan front (Fig. 5.6-6) or eastern Andean foreland thrust belt (Fig. 5.6-10) have fault planes that rotate as the trend of the mountains changes, suggesting that the fault planes are controlled by the existing structures, so the P axes only partially reflect the stress field. A similar pattern appears for T axes along the East African rift (Fig. 5.6-2). In general, stress axes inferred from many fault plane solutions in an area seem relatively coherent (Fig. 5.6-19). Thus we assume that the crust contains preexisting faults of all orientations, so the average stress orientation inferred from the focal mechanisms is not seriously biased.

At this point, it is worth noting other complexities. Both the failure and sliding curves may be more complicated than straight lines. These curves, known as Mohr envelopes, can be derived from experiments at various values of stress. Additional complexity comes from the fact that water and other fluids are often present in rocks, especially in the upper crust. The fluid pressure, known as the *pore pressure*, reduces the effect of the normal stress and allows sliding to take place at lower shear stresses. This effect is modeled by replacing the normal stress  $\sigma$  with  $\bar{\sigma} = \sigma - P_f$ , known as the *effective normal stress*, where  $P_f$  is the pore fluid pressure.<sup>2</sup> Because the pore pressure is defined as negative, the effective normal stress is reduced (less compressive). Similarly, effective principal stresses taking into account pore pressure,

$$\bar{\sigma}_1 = \sigma_1 - P_f \quad \text{and} \quad \bar{\sigma}_2 = \sigma_2 - P_f, \quad (16)$$

are used in the fracture theory.

The relations we have discussed can be used to estimate the maximum stresses that the crust can support. Laboratory experiments (Fig. 5.7-10) for sliding on existing faults in a variety of rock types find relations sometimes called *Byerlee's law*:

$$\begin{aligned} \tau &\approx -0.85\bar{\sigma}, \quad |\bar{\sigma}| < 200 \text{ MPa} \\ \tau &\approx 50 - 0.6\bar{\sigma}, \quad |\bar{\sigma}| > 200 \text{ MPa}. \end{aligned} \quad (17)$$

These relations, written in terms of the normal and shear stresses on a fault, can be used to infer the principal stress as a function of depth. To do so, we write the minimum compressive stress as  $\sigma_3$ , because we are in three dimensions. We assume that the crust contains faults of all orientations, and that the stresses cannot exceed the point where Mohr's circle is tangent to the frictional sliding line, or else sliding will occur (Fig. 5.7-11). At shallow depths where  $|\bar{\sigma}| < 200$  MPa, Eqn 17 shows that  $\tau_0 = 0$ . Thus Eqn 13, the relation between the stresses when fracture occurs, yields

$$\bar{\sigma}_1 = \bar{\sigma}_3 \tan^2 \theta_s. \quad (18)$$

Using Eqn 7 for the case of frictional sliding,

$$\theta_s = \alpha/2 + 45^\circ, \quad (19)$$

and the values in Eqn 17 give

$$\mu = \tan \alpha = 0.85, \quad \alpha \approx 41^\circ, \quad \theta_s \approx 66^\circ, \quad \tan^2 66^\circ \approx 5, \quad (20)$$

so the stresses are related by

$$\bar{\sigma}_1 \approx 5\bar{\sigma}_3. \quad (21)$$

At greater depths, where  $|\bar{\sigma}| > 200$  MPa,  $\alpha \approx 31^\circ$  and  $\theta_s = 60.5^\circ$ , so the stresses are related by

$$\bar{\sigma}_1 \approx -175 + 3.1\bar{\sigma}_3. \quad (22)$$

<sup>2</sup> The role of pore pressure in making sliding easier can be seen by trying to slide an object across a dry table and then wetting the table.

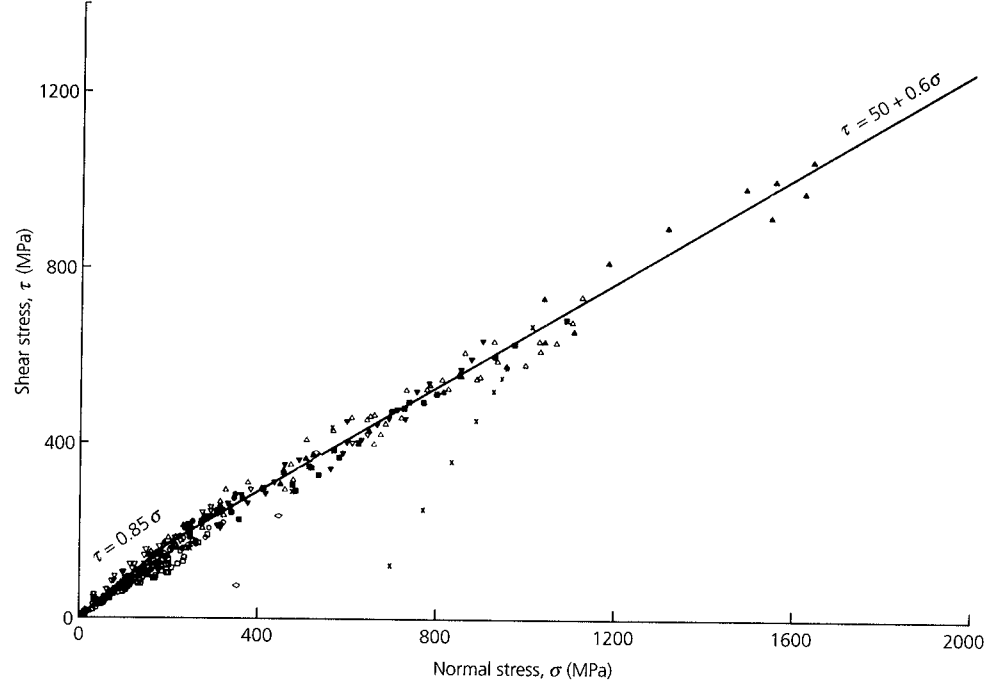


Fig. 5.7-10 Shear stress versus normal stress for frictional sliding, compiled for various rock types. Compressive stress is positive. (Byerlee, 1978. *Pure Appl. Geophys.*, 116, 615–26, reproduced with the permission of Birkhäuser.)

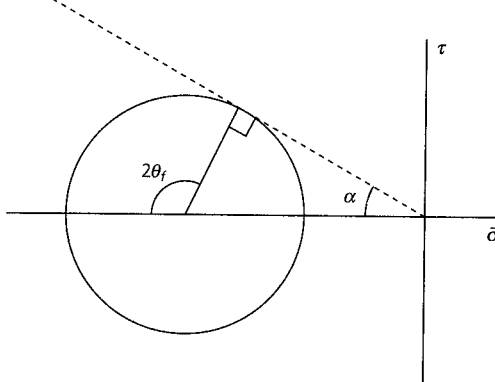


Fig. 5.7-11 Mohr's circle and sliding line for  $|\bar{\sigma}| < 200$  MPa. If the lithosphere contains fractures in all directions, the stresses cannot exceed those at the point where Mohr's circle is tangent to the sliding line, because sliding would occur.

We assume that one principal stress,  $\sigma_1$  or  $\sigma_3$ , is the vertical stress due to the lithostatic pressure as a function of depth ( $z$ ),

$$\sigma_V = -\rho g z. \quad (23)$$

The other principal stress, which must be horizontal, is denoted  $\sigma_H$ . The pore pressure  $P_f(z)$  is unknown. One common assumption is that the rock is dry, so  $P_f(z) = 0$ . Another is that the pore pressure is *hydrostatic*, which is equivalent to assuming that pores are connected up to the surface, so

$$P_f(z) = -\rho_f g z, \quad (24)$$

where  $\rho_f$  is the density of the fluid, which is usually water, with  $\rho_f = 1$  g/cm<sup>3</sup>. Alternatively, the pore pressure can be assumed to be a fixed fraction of the lithostatic pressure (Section 2.3.6).

We now can find the *strength* of the crust, defined by the maximum difference between the horizontal and vertical stresses that the rock can support. At shallow depths where  $|\bar{\sigma}| < 200$  MPa, Eqn 21 shows that  $\bar{\sigma}_1 = 5\bar{\sigma}_3$ . There are two possibilities, depending on whether the vertical stress is the most ( $\sigma_1$ ) or least ( $\sigma_3$ ) compressive. If the vertical stress is the most compressive,

$$\begin{aligned} \sigma_V &= \sigma_1, & \bar{\sigma}_1 &= \sigma_V - P_f = -\rho g z - P_f(z) \\ \sigma_H &= \sigma_3, & \bar{\sigma}_3 &= \sigma_1/5 = -(\rho g z + P_f(z))/5. \end{aligned} \quad (25)$$

Alternatively, if the vertical stress is the least compressive,

$$\begin{aligned} \sigma_V &= \sigma_3, & \bar{\sigma}_3 &= \sigma_V - P_f = -\rho g z - P_f(z) \\ \sigma_H &= \sigma_1, & \bar{\sigma}_1 &= 5\bar{\sigma}_3 = -5(\rho g z + P_f(z)). \end{aligned} \quad (26)$$

In the first case,

$$\sigma_H - \sigma_V = \sigma_3 - \sigma_1 = 0.8(\rho g z + P_f(z)), \quad (27)$$

corresponds to an extensional (positive) stress. In the second,

$$\sigma_H - \sigma_V = \sigma_1 - \sigma_3 = -4(\rho g z + P_f(z)) \quad (28)$$

corresponds to a compressive (negative) stress that is much greater in absolute value. Thus, at any depth, the crust can

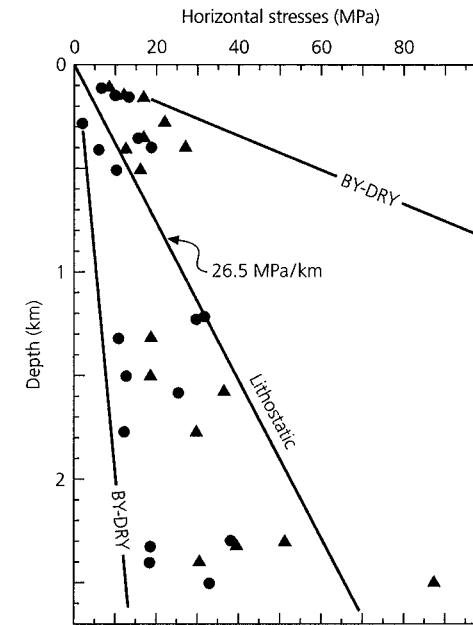


Fig. 5.7-12 Horizontal stresses measured in southern Africa. Dots are for horizontal stresses being the least compressive ( $\bar{\sigma}_3$ ), and triangles are for horizontal stresses being the most compressive ( $\bar{\sigma}_1$ ). The lithostatic stress gradient (26.5 MPa/km) is shown, along with Byerlee's law (BY) for zero pore pressure (DRY). The stronger line is for compression, and the weaker one is for extension. The observed stresses are within the maximum and minimum BY-DRY lines. (Brace and Kohlstedt, 1980. *J. Geophys. Res.*, 85, 6248–52, copyright by the American Geophysical Union.)

support greater compressive deviatoric stress than extensional deviatoric stress (Fig. 5.7-12).

### 5.7.3 Ductile flow

When rocks behave brittlely, their behavior is not time-dependent; they either strain elastically or fail. By contrast, the deformation of ductile rock depends on time. A common model for the time-dependent behavior is a *Maxwell viscoelastic material*, which behaves like an elastic solid on short time scales and like a viscous fluid on long time scales. This model can describe the mantle because seismic waves propagate as though the mantle were solid, whereas postglacial rebound and mantle convection occur as though the mantle were fluid.

To see this difference, consider two types of deformation in one dimension. For an elastic solid subjected to elastic strain  $e_E = e_{11}$ ,

$$\sigma = E e_E, \quad (29)$$

where  $E$  is Young's modulus, and  $\sigma$  is  $\sigma_{11}$ . The simplest viscous fluid obeys

$$\sigma = 2\eta \frac{de_F}{dt}, \quad (30)$$

where  $\eta$  is the viscosity, and  $e_F$  is the fluid portion of the strain. This equation defines the viscosity, the property that measures a fluid's resistance to shear.<sup>3</sup>

We often think of an elastic material as a spring, which exerts a force proportional to distance. Thus stress and strain are proportional at any instant, and there are no time-dependent effects. By contrast, the viscous material is thought of as a dashpot, a fluid damper that exerts a force proportional to velocity. Hence the stress and strain rate are proportional, and the material's response varies with time. These effects are combined in a viscoelastic material, which can be thought of as a spring and dashpot in series (Fig. 5.7-13). The combined elastic and viscous response comes from the combined strain rate

$$\frac{de}{dt} = \frac{de_E}{dt} + \frac{de_F}{dt} = \frac{1}{E} \frac{d\sigma}{dt} + \frac{\sigma}{2\eta}. \quad (31)$$

This differential equation, the rheological law for a Maxwell substance, shows how the stress in the material evolves after a strain  $e_o$  is applied at time  $t = 0$  and then remains constant. At  $t = 0$  the derivative terms dominate, so the material behaves elastically, and has an initial stress

$$\sigma_o = E e_o. \quad (32)$$

For  $t > 0$ ,  $de/dt = 0$ , so

$$\frac{d\sigma}{dt} = -\frac{E}{2\eta} \sigma, \quad (33)$$

whose integral is

$$\sigma(t) = \sigma_o \exp [-(Et/2\eta)]. \quad (34)$$

Thus stress relaxes from its initial value as a function of time (Fig. 5.7-13). A useful parameter is the *Maxwell relaxation time*,<sup>4</sup>

$$\tau_M = \frac{2\eta}{E} \approx \frac{\eta}{\mu}, \quad (35)$$

required for the stress to decay to  $e^{-1}$  of its initial value. For times less than  $\tau_M$  the material can be considered an elastic solid, whereas for longer times it can be considered a viscous fluid.

For example, if the mantle is approximately a Poisson solid with  $\mu \approx 10^{12}$  dyn/cm<sup>2</sup> and  $\eta \approx 10^{22}$  poise, its Maxwell time is about  $10^{10}$  s or 300 years. Although the viscosity is not that well known, so estimates of the Maxwell time vary, it is clear

<sup>3</sup> In familiar terms, viscosity measures how “gooey” a fluid is. Maple syrup is somewhat more viscous than water, and the earth's mantle is about  $10^{24}$  times more viscous.

<sup>4</sup> Definitions of the Maxwell time vary, but always involve the ratio of the viscosity to an elastic constant.

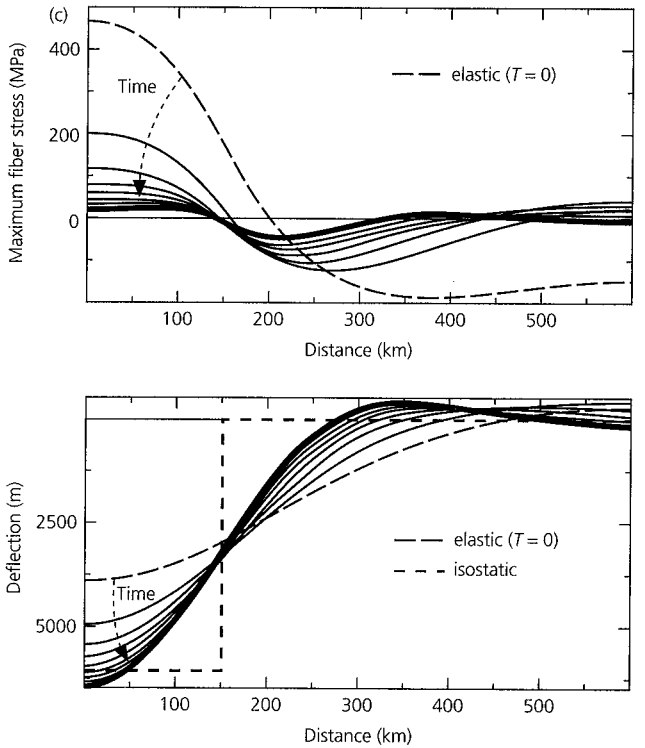


**Fig. 5.7-13** (a) Model of a viscoelastic material as an elastic spring and viscous dashpot in series. (b) Stress response of a viscoelastic material to an applied strain. The Maxwell relaxation time,  $\tau_M$ , is the time the stress takes to decay to  $e^{-1}$  of its initial value. (c) Evolution of the deflection and bending stress produced by a sediment load on a viscoelastic earth. At first the earth responds elastically, as shown by the long-dashed line, but with time it flows, so the deflection beneath the load deepens and the stresses relax. (Stein *et al.*, 1989, with kind permission from Kluwer Academic Publishers.)

that we can treat the mantle as a solid for seismological purposes and as a fluid in tectonic modeling. If we model the mantle as viscoelastic, then a load applied on the surface has an effect that varies with time. Figure 5.7-13c shows the effect of a 150 km-wide sediment load, as might be expected on a passive continental margin. Initially, the earth responds elastically, causing large flexural bending stresses. With time, the mantle flows, so the deflection beneath the load deepens and the stresses relax. In the time limit, the stress goes to zero, and the deflection approaches the isostatic solution, because isostasy amounts to assuming that the lithosphere has no strength. Stress relaxation may explain why large earthquakes are rare at continental margins, except where glacial loads have been recently removed (Fig. 5.6-20). Although the large sediment loads should produce stresses much greater than other sources of intraplate stress, including the smaller and less dense ice loads, the stresses produced by sediment loading early in the margin's history may have relaxed.

Laboratory experiments indicate that the rheology of minerals in ductile flow can be described by

$$\frac{de}{dt} = \dot{\epsilon} = f(\sigma) A \exp [-(E^* + PV^*)/RT], \quad (36)$$

where  $T$  is temperature,  $R$  is the gas constant, and  $P$  is pressure.  $f(\sigma)$  is a function of the stress difference  $|\sigma_1 - \sigma_3|$ , and  $A$  is a constant. The effects of pressure and temperature are described by the *activation energy*  $E^*$  and the *activation volume*  $V^*$ . Observed values of  $f(\sigma)$  are often fit well by assuming

$$f(\sigma) = |\sigma_1 - \sigma_3|^n \quad (37)$$

$$\dot{\epsilon} = |\sigma_1 - \sigma_3|^n A \exp [-(E^* + PV^*)/RT]. \quad (38)$$

The rheology of such fluids is characterized by a power law. If  $n = 1$ , the material is called *Newtonian*, whereas a non-Newtonian fluid with  $n = 3$  is often used to represent the mantle. From Eqn 30 we see that for a Newtonian fluid the viscosity depends on both temperature and pressure:

$$\eta = (1/2A) \exp [(E^* + PV^*)/RT]. \quad (38)$$

Thus the viscosity decreases exponentially with temperature. This decrease is assumed to give rise to a strong lithosphere overlying a weaker asthenosphere, and the restriction of earthquakes to shallow depths.<sup>5</sup> For a non-Newtonian fluid, Eqn 30 gives the *effective viscosity*, the equivalent viscosity if the fluid were Newtonian.

We think of equations like Eqn 37 as showing the strength, or maximum stress difference  $|\sigma_1 - \sigma_3|$ , that the viscous material can support. This stress difference depends on temperature, pressure, strain rate, and rock type. The material

<sup>5</sup> Temperature-dependent viscosity is an effect familiar to automobile drivers in cold temperatures, when the engine and the transmission became noticeably sluggish.

is stronger at higher strain rates, and weakens exponentially with high temperatures. At shallow depths, the small pressure effect is often neglected, so the activation volume  $V^*$  is treated as zero. For example, a commonly used flow law for dry olivine is<sup>6</sup>

$$\dot{\epsilon} = 7 \times 10^4 |\sigma_1 - \sigma_3|^3 \exp \left( \frac{-0.52 \text{ MJ/mol}}{RT} \right) \quad \text{for } |\sigma_1 - \sigma_3| \leq 200 \text{ MPa}$$

$$= 5.7 \times 10^{11} \exp \left[ \frac{-0.54 \text{ MJ/mol}}{RT} \left( 1 - \frac{[\sigma_1 - \sigma_3]^2}{8500} \right) \right] \quad \text{for } |\sigma_1 - \sigma_3| > 200 \text{ MPa}, \quad (39)$$

where  $\dot{\epsilon}$  is in  $s^{-1}$ . Similarly, for quartz,

$$\dot{\epsilon} = 5 \times 10^6 |\sigma_1 - \sigma_3|^3 \exp \left( \frac{-0.19 \text{ MJ/mol}}{RT} \right) \quad \text{for } |\sigma_1 - \sigma_3| < 1000 \text{ MPa}. \quad (40)$$

At a given strain rate, quartz is much weaker (can sustain a smaller stress difference) than olivine. Thus the quartz-rich continental crust should be weaker than the olivine-rich oceanic crust, an effect whose tectonic consequences are discussed next.

#### 5.7.4 Strength of the lithosphere

The strength of the lithosphere as a function of depth depends upon the deformation mechanism. At shallow depths, rocks fail by either brittle fracture or frictional sliding on preexisting faults. Both processes depend in a similar way on the normal stress, with rock strength increasing with depth. However, at greater depths the ductile flow strength of rocks is less than the brittle or frictional strength, so the strength is given by the flow laws and decreases with depth as the temperatures increase. This temperature-dependent strength is the reason why the cold lithosphere forms the planet's strong outer layer.

To calculate the strength, a strain rate and a geotherm giving temperature as a function of depth are assumed. At shallow depths the strength, the maximum stress difference before frictional sliding occurs, is computed using Eqns 27 and 28. At some depth, the frictional strength exceeds the ductile strength allowed by the flow law, so for deeper depths the maximum strength is given by the flow law. Figure 5.7-14 shows a strength plot, known as a *strength envelope*, for a strain rate of  $10^{-15} \text{ s}^{-1}$  and a temperature gradient appropriate for old oceanic lithosphere or stable continental interior. In the frictional region, curves are shown for various values of  $\lambda$ , the ratio of pore pressure to lithostatic pressure. The higher

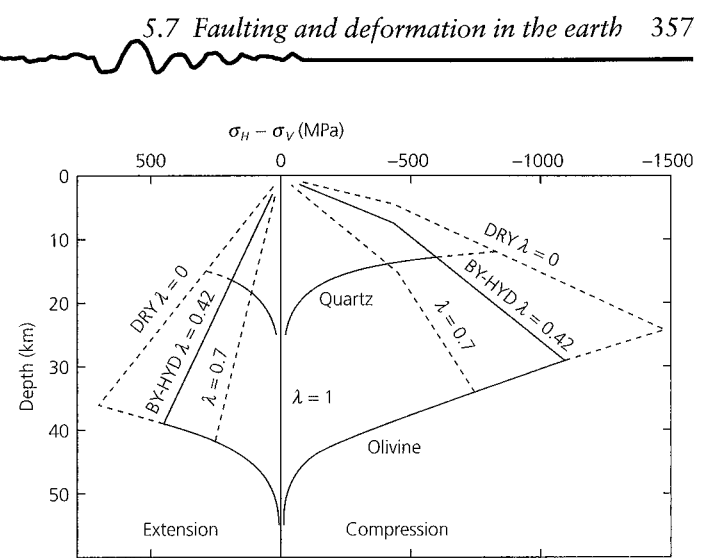


**Fig. 5.7-14** Strength envelopes as a function of depth for various values of  $\lambda$ , the ratio of pore pressure to lithostatic pressure. BY-HYD lines are for Byerlee's law with hydrostatic pore pressure. At shallow depths, strength is controlled by brittle fracture; at greater depths ductile flow laws predict rapid weakening. In the ductile flow regime, quartz is weaker than olivine. In the brittle regime, the lithosphere is stronger in compression (right side) than in extension (left side). (Brace and Kohlstedt, 1980. *J. Geophys. Res.*, 85, 6248–52, copyright by the American Geophysical Union.)

pore pressures result in lower strengths. Ductile flow laws are shown for quartz and olivine, minerals often used as models for continental and oceanic rheologies. Strength increases with depth in the brittle region, due to the increasing normal stress, and then decreases with depth in the ductile region, due to increasing temperature. Hence strength is highest at the *brittle-ductile transition*. Strength decreases rapidly below this transition, so the lithosphere should have little strength at depths greater than about 25 km in the continents and 50 km in the oceans. The strength envelopes show that the lithosphere is stronger for compression than for tension in the brittle regime, but the two are symmetric in the ductile regime. Strength envelopes are often plotted using the rock mechanics convention of compression positive.

The actual distribution of strength with depth is probably more complicated, because the brittle-ductile transition occurs over a region of semi-brITTLE behavior that includes both brittle and plastic processes (Fig. 5.7-3). However, this simple model gives insight into various observations. In particular, we have seen that the depths of earthquakes in several tectonic environments seem to be limited by temperature. This makes sense, because for a given strain rate and rheology the exponential dependence on temperature would make a limiting strength for seismicity approximate a limiting temperature.

To see this, consider Fig. 5.7-15, which shows that as oceanic lithosphere ages and cools, the predicted strong region deepens. This result seems plausible because earthquake depths, seismic velocities, and effective elastic thicknesses imply that the strong upper part of the lithosphere thickens with age (Fig. 5.3-9). The strength envelopes are thus consistent with the observation that the maximum depth of earthquakes within

<sup>6</sup> Brace and Kohlstedt (1980).

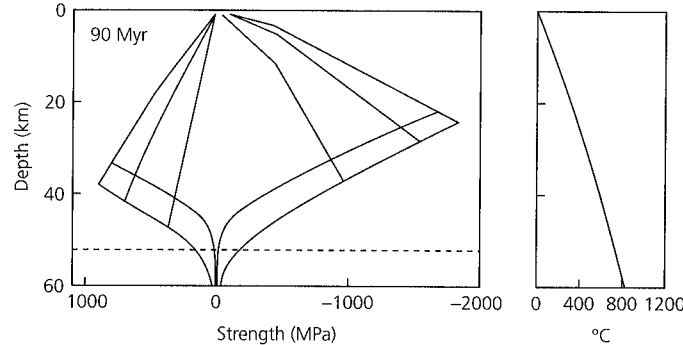
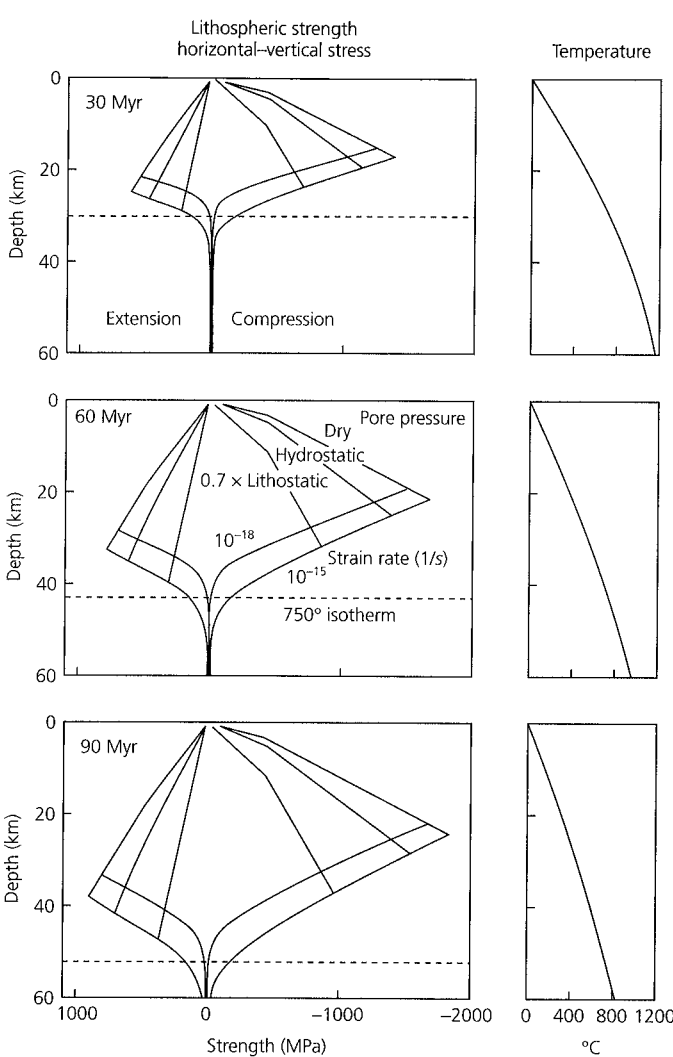


**Fig. 5.7-15** Strength envelopes showing maximum stress difference (strength) as a function of depth for an olivine rheology, for geotherms (right) corresponding to cooling oceanic lithosphere of different ages. Strength in the brittle regime is reduced by higher pore pressure; strength in the ductile regime is reduced by lower strain rate. The depth range in which the material is strong enough for faulting increases with age. (Wiens and Stein, 1983. *J. Geophys. Res.*, 88, 6455–68, copyright by the American Geophysical Union.)

the oceanic lithosphere is approximately bounded by the 750°C isotherm (Fig. 5.7-16). These envelopes are drawn for strain rates of  $10^{-15}$  and  $10^{-18} \text{ s}^{-1}$ , appropriate for slow deformation within plates. By contrast, a seismic wave with a period of 1 s, a wavelength of 10 km, and a displacement of  $10^{-6} \text{ m}$  corresponds to a strain rate of  $10^{-10} \text{ s}^{-1}$ . The successively greater effective elastic thicknesses, depth of the deepest earthquakes, and depth of the low-velocity zone are thus consistent with strength increasing with strain rate.

The strength envelopes give insight into differences between continental and oceanic lithospheres (Fig. 5.7-17). First, quartz is weaker than olivine at a given temperature (Fig. 5.7-14),

**Fig. 5.7-16** Plots of strength and seismicity versus temperature. The strength envelopes explain the observation that intraplate oceanic seismicity occurs only above the 750°C isotherm. (Wiens and Stein, 1985. *Tectonophysics*, 116, 143–62, with permission from Elsevier Science.)

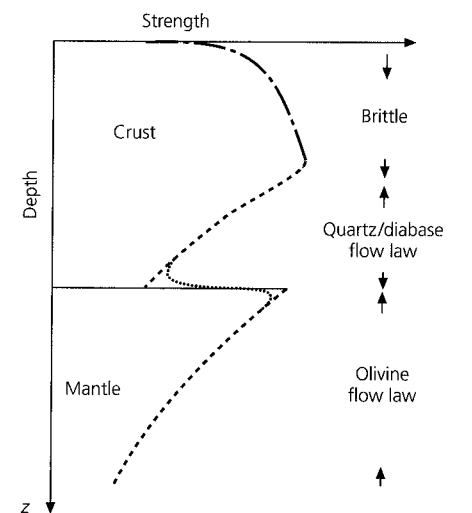


**Fig. 5.7-17** Schematic strength envelope for continents. Below the ductile lower crust may be a stronger zone in the olivine-rich mantle. (Chen and Molnar, 1983. *J. Geophys. Res.*, 88, 4183–4214, copyright by the American Geophysical Union.)

consistent with the fact that the limiting temperature for continental seismicity is lower than for oceanic earthquakes (Fig. 5.7-18). Second, the strength profiles differ. The strength of oceanic lithosphere increases with depth and then decreases. However, in continental lithosphere we expect such a profile in

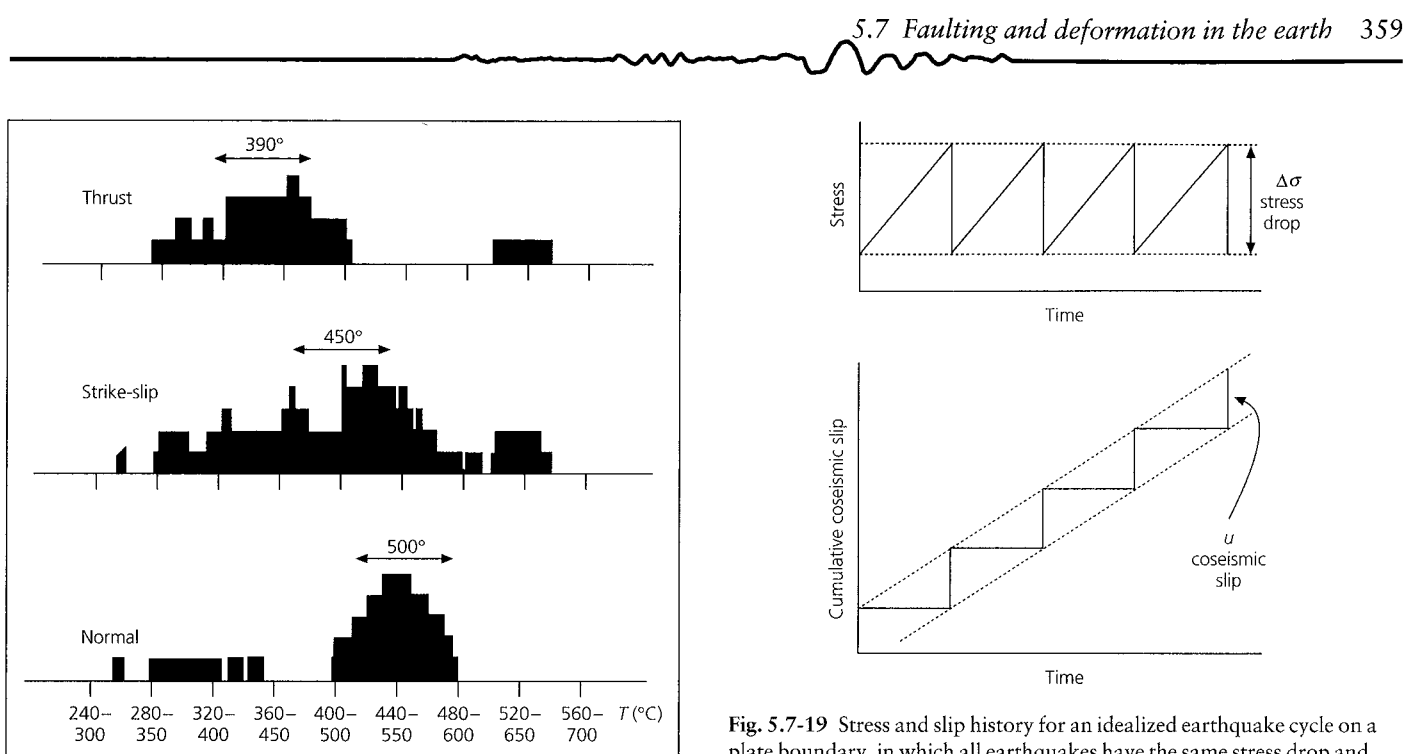


**Fig. 5.7-18** Limiting temperatures for continental seismicity. These temperatures are much lower than those for oceanic lithosphere, since the quartz rheology in continents is much weaker than olivine. (Courtesy of J. Strehlau and R. Meissner.)

the quartz-rich crust, but also a second, deeper zone of strength below the Moho, due to the olivine rheology. This ‘jelly sandwich’ profile including a weak zone may be part of the reason why continents deform differently than oceanic lithosphere. For example, some continental mountain building (Fig. 5.6-6) may involve crustal thickening in which slices of upper crust, which are too buoyant to subduct, are instead thrust atop one another. The weaker lower crust may also contribute in other ways to the general phenomenon that continental plate boundaries are broader and more complex than their oceanic counterparts (Fig. 5.2-4).

### 5.7.5 Earthquakes and rock friction

It is natural to assume that earthquakes occur when tectonic stress exceeds the rock strength, so a new fault forms or an existing one slips. Thus steady motion across a plate boundary seems likely to give rise to a cycle of successive earthquakes at regular intervals, with the same slip and stress drop (Fig. 5.7-19). However, we have seen that the earthquake process is more complicated. The time between earthquakes on plate boundaries varies (Fig. 1.2-15), although the plate motion causing the earthquakes is steady. Earthquakes sometimes rupture along the same segments of a boundary as in earlier earthquakes, and other times along a different set (Fig. 5.4-27). Moreover, many large earthquakes show a complicated rupture pattern, with some parts of the fault releasing more seismic energy than others (Fig. 4.5-10). Attempts to understand these

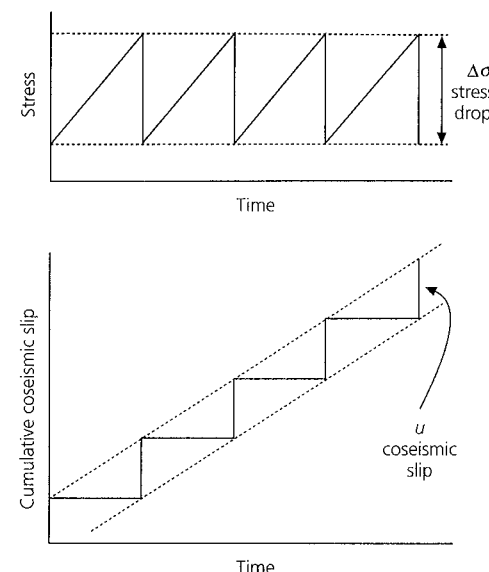


**Fig. 5.7-19** Stress and slip history for an idealized earthquake cycle on a plate boundary, in which all earthquakes have the same stress drop and coseismic slip. (Shimazaki and Nakata, 1980. *Geophys. Res. Lett.*, 7, 279–82, copyright by the American Geophysical Union.)

complexities often combine two basic themes. Some of the complexity may be due to intrinsic randomness of the failure process, such that some small ruptures cascade into large earthquakes, whereas others do not (Section 1.2.6). Other aspects of the complexity may be due to features of rock friction.

Interesting insight emerges from considering an experiment in which stress is applied until a rock breaks. When the fault forms, some of the stress is released, and then motion stops. If stress is reapplied, another stress drop and motion occur once the stress reaches a certain level. So long as stress is reapplied, this pattern of jerky sliding and stress release continues (Fig. 5.7-20).

This pattern, called *stick-slip*, looks like a laboratory version of what happens in a sequence of earthquakes on a fault. By this analogy, the stress drop in an earthquake relieves only part of the total tectonic stress, and as the fault continues to be loaded by tectonic stress, occasional earthquakes occur. The analogy is strengthened by the fact that at higher temperatures (about 300° for granite), stick-slip does not occur (Fig. 5.7-20). Instead, *stable sliding* occurs on the fault, much as earthquakes do not occur at depths where the temperature exceeds a certain value. Thus, understanding stick-slip in the laboratory seems likely to give insight into the earthquake process.

Stick-slip results from a familiar phenomenon: it is harder to start an object sliding against friction than to keep it going once it is sliding. This is because the *static friction* stopping the object from sliding exceeds the *dynamic friction* that opposes motion once sliding starts.<sup>7</sup> To understand how this difference

<sup>7</sup> This effect is the basis of cross-country skiing, where loading one ski makes it grip the snow, while unloading the other lets it glide.

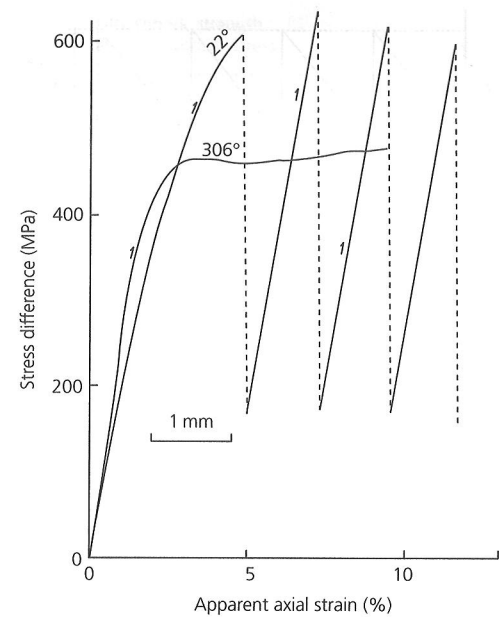


Fig. 5.7-20 Force versus slip history for a rock sample. At low temperature, so long as stress is reapplied, a stick-slip pattern of jerky sliding and stress release continues. By contrast, stable sliding occurs at high temperature. (Brace and Byerlee, 1970. *Science*, 168, 1573–5, copyright 1970 American Association for the Advancement of Science.)

causes stick-slip, and get insight into stick-slip as a model for earthquakes, consider the experiment in Fig. 5.7-21. It turns out that if an object is pulled across a table with a rubber band, jerky stick-slip motion occurs.<sup>8</sup> Thus a steady load, combined with the difference in static and dynamic friction, causes an instability and a sequence of discrete slip events.

We analyze this situation assuming that a block (sometimes called a slider) is loaded by a spring that applies a force  $f$  proportional to the spring constant (stiffness)  $k$  and the spring extension. If the loading results from the spring's far end moving at a velocity  $v$ , the spring force is

$$f = k(\zeta + vt - u), \quad (41)$$

where  $u$  is the distance the block slipped, and  $\zeta$  is the spring extension when sliding starts at  $t = 0$ . This motion is opposed by a frictional force  $|\tau| = -\mu\sigma$  equal to the product of  $\sigma$ , the compressive (negative) normal stress due to the block's weight, and the friction coefficient,  $\mu$ . By Newton's second law that force equals mass times acceleration,

$$m \frac{d^2u}{dt^2} = f - \tau = k(\zeta + vt - u) + \mu\sigma. \quad (42)$$

<sup>8</sup> We suggest trying this experiment.

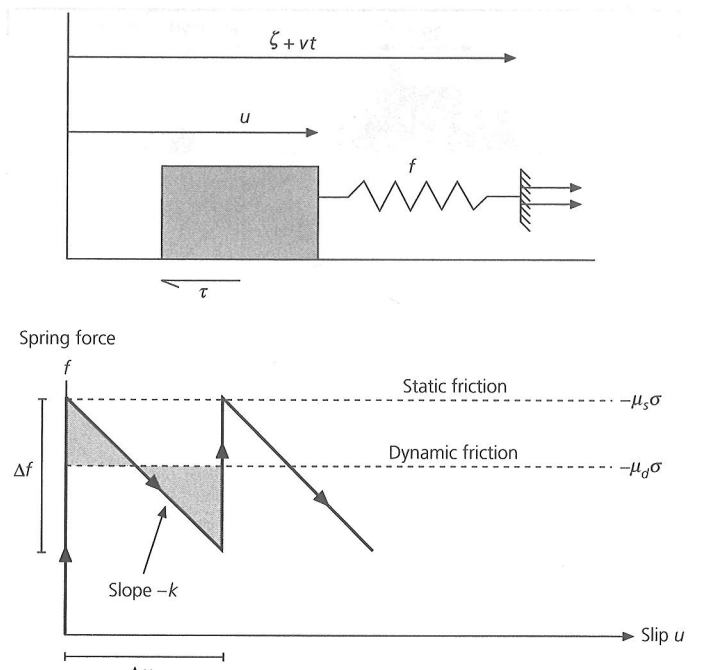


Fig. 5.7-21 A simple spring and slider block analog for stick-slip as a model for earthquakes. The slider is loaded by force  $f$  due to the spring end moving at velocity  $v$ . Before sliding, the block is retarded by a static friction force  $\tau = -\mu_s \sigma$ , but once sliding starts, the friction force decreases to  $-\mu_d \sigma$ . A series of slip events occur, each with slip  $\Delta u$  and force change (stress drop)  $\Delta f$ .

However, the block starts sliding only once the spring force exceeds the frictional force, so just before sliding starts at  $t = 0$ ,

$$0 = k\zeta + \mu_s\sigma, \quad (43)$$

where  $\mu_s$  is the static friction coefficient. For simplicity, assume that at the instant sliding starts, the friction drops to its dynamic value  $\mu_d$ , and

$$m \frac{d^2u}{dt^2} = k(\zeta - u) + \mu_d\sigma. \quad (44)$$

Subtracting Eqn 43 from Eqn 44 gives

$$m \frac{d^2u}{dt^2} = -ku + (\mu_d - \mu_s)\sigma = -ku + \Delta\mu\sigma, \quad (45)$$

which we can use as the equation of motion for the block's slip history  $u(t)$  if the loading rate  $v$  is slow enough to ignore during the slip event.

A solution to Eqn 45, with initial conditions  $u(0) = 0$  and  $\frac{du(0)}{dt} = 0$ , is

$$\begin{aligned} u(t) &= \frac{\Delta\mu\sigma}{k} (1 - \cos \omega t) \quad (\text{slip}), \\ \frac{du(t)}{dt} &= \frac{\Delta\mu\sigma}{\sqrt{km}} \sin \omega t \quad (\text{velocity}), \\ \frac{du^2(t)}{dt^2} &= \frac{\Delta\mu\sigma}{m} \cos \omega t \quad (\text{acceleration}), \end{aligned} \quad (46)$$

where  $\omega = \sqrt{k/m}$ . As shown, the block starts slipping because the spring force exceeds the friction force. During the slip event, the spring force decreases as the spring shortens, until it becomes less than the friction force and the block slows and eventually stops. The block stops once the shaded area above the spring force line equals that below the line, or when the work done accelerating the block equals that which decelerated it. If the spring end continues to move, loading continues until the spring force again equals the static friction force and another slip event occurs.

It is interesting to think of analogies between this model of slip events and earthquakes. The slip event's duration  $t_D$ , analogous to an earthquake rise time (Section 4.3.2), satisfies

$$\frac{du(t_D)}{dt} = 0, \quad t_D = \frac{\pi}{\omega} = \pi\sqrt{m/k}. \quad (47)$$

The total slip during the event is

$$\Delta u = u(t_D) = 2\Delta\mu\sigma/k, \quad (48)$$

and the drop in the spring force, which is analogous to an earthquake stress drop (Section 4.6.3), is

$$\Delta f = 2\Delta\mu\sigma. \quad (49)$$

Thus the rise time depends on the spring constant, but not on the difference between static and dynamic friction. However, the total slip and stress drop depend upon the friction difference. None of these depend upon the loading rate, which is analogous to the rate of plate motion causing earthquakes on a plate boundary. But the loading rate determines the time between successive slip events. Thus, in the plate boundary analogy, the time between large earthquakes depends on the plate motion rate, but their slip and stress drop depend on the frictional properties of the fault and the normal stress. Hence faster-slipping boundaries would have more frequent large earthquakes, but the slip and stress drop in them would not be greater than on a slower boundary with similar frictional properties and normal stress.

Laboratory experiments show that the difference between static and dynamic friction is more complicated than the constant values assumed in this simple model. We can think of the lower dynamic friction as showing either velocity weakening, decreasing as the object moves faster, or slip weakening, decreasing as the object moves further. Frictional models called

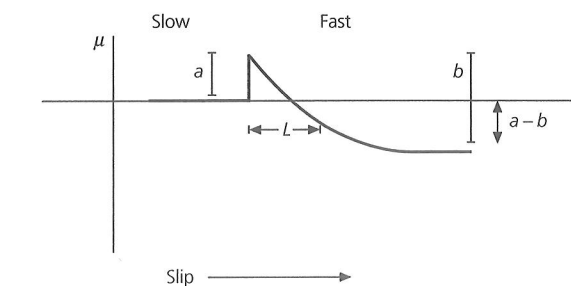


Fig. 5.7-22 Evolution of friction in a simple rate- and state-dependent model. If the slip rate increases by a factor of  $e$ , friction increases by  $a$ , and then decreases as slip progresses to a steady-state value  $a - b$ . (After Scholz, 1990. Reprinted with the permission of Cambridge University Press.)

rate- and state-dependent friction with a variable coefficient of sliding friction,  $\mu$ , are used to describe these effects. In a simple model of this sort,

$$\mu = [\mu_0 + b\psi + a \ln(v/v^*)], \quad (50)$$

where  $\mu_0$  is the coefficient of static friction. The friction depends on the slip rate  $v$ , normalized by a rate  $v^*$ , and a state variable  $\psi$  that represents the slip history

$$\frac{d\psi}{dt} = -(v/L)[\psi + \ln(v/v^*)], \quad (51)$$

where  $L$  is an experimentally determined characteristic distance. The friction also depends on  $a$  and  $b$ , which characterize the material.

Figure 5.7-22 illustrates how friction evolves. If the slip rate increases by a factor of  $e$ , the friction increases by  $a$ , and then decreases as slip progresses, reaching a new steady-state value. With time,  $\psi$  reaches a steady-state value given by Eqn 51,

$$0 = -(\nu/L)[\psi_{ss} + \ln(\nu/\nu^*)], \quad \psi_{ss} = -\ln(\nu/\nu^*). \quad (52)$$

The steady state friction (Eqn 50) is

$$\mu_{ss} = [\mu_0 + b\psi_{ss} + a \ln(\nu/\nu^*)] = [\mu_0 + (a - b) \ln(\nu/\nu^*)], \quad (53)$$

and varies with slip rate as

$$\frac{d\mu_{ss}}{d \ln v} = (a - b), \quad (54)$$

so after the slip velocity change, the net friction change is  $(a - b)$ . If  $(a - b)$  is negative, the material shows velocity weakening, which permits earthquakes to occur by stick-slip. However, for  $(a - b)$  positive, the material shows velocity strengthening, and stable sliding is expected. Laboratory results (Fig. 5.7-20) show that  $a - b$  for granite changes sign at about  $300^\circ$ , which should be the limiting temperature for earthquakes. Thus the frictional

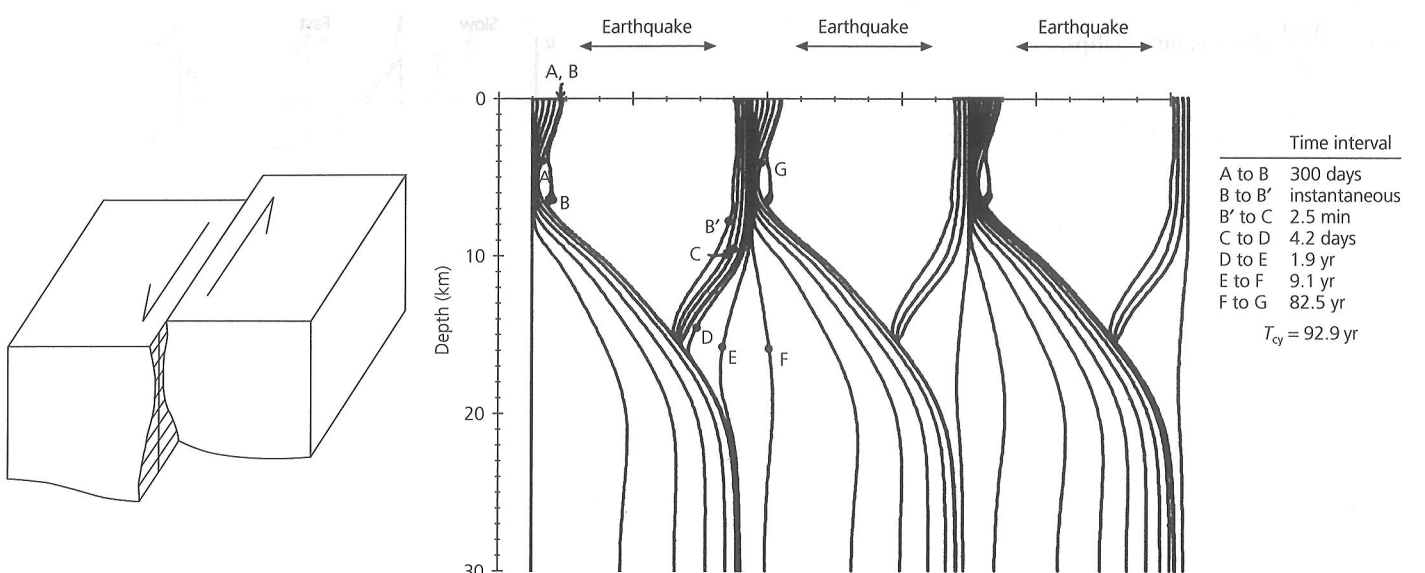


Fig. 5.7-23 Earthquake cycle for a model in which a strike-slip fault with rate- and state-dependent frictional properties is loaded by plate motion. The slip history for three cycles as a function of depth and time is shown by the lines, each of which represents a specific time. Steady motion occurs at depth, and stick-slip occurs above 11 km. (After Tse and Rice, 1986. *J. Geophys. Res.*, 91, 9452–72, copyright by the American Geophysical Union.)

model predicts a maximum depth for continental earthquakes similar to that predicted by the rock strength arguments.

These results can be used to simulate the earthquake cycle, using fault models analogous to the simple slider model (Fig. 5.7-21). Figure 5.7-23 shows the slip history as a function of depth and time for a model in which a strike-slip fault is loaded by plate motion. The fault is described by rate- and state-dependent frictional properties as a function of depth, such that stick-slip occurs above 11 km. Initially from time A to B, stable sliding occurs at depth, and a little precursory slip occurs near the surface. The earthquake causes 2.5 m of sudden slip at shallow depths, as shown by the curves for times B and B'. As a result, the faulted shallow depths "get ahead" of the material below, loading that material and causing postseismic slip from times B' to F. Once this is finished, the 93-year cycle starts again with steady stable sliding at depth.

Such models replicate many aspects of the earthquake cycle. An interesting difference, however, is that the models predict earthquakes at regular intervals, whereas earthquake histories are quite variable. Some of the variability may be due to the effects of earthquakes on other faults, or other segments of the same fault. Figure 5.7-24 shows this idea schematically for the slider model in Fig. 5.7-21. Assume that after an earthquake cycle, the compressive normal stress  $\sigma$  on the slider is reduced. This "unclamping" reduces the frictional force resisting sliding, so it takes less time for the spring force to rise again to the level needed for the next slip event. Conversely, increased compression "clamps" the slider more, and so increases the time until the next slip event. In addition, by Eqn 49, the stress drop in the slip event changes when  $\sigma$  changes.

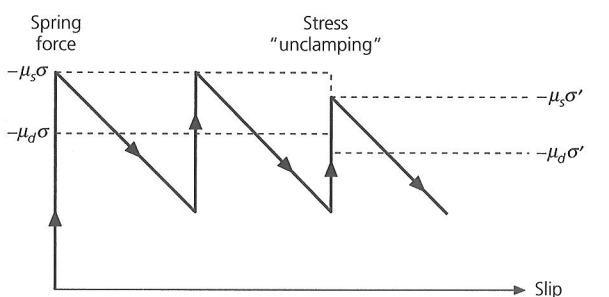


Fig. 5.7-24 Modification of a slider block model (Fig. 5.7-21) to include the effects of changes in normal stress. Reduced normal stress ( $|\sigma| < |\sigma'|$ ) reduces the frictional force, and so "unclamps" the fault and decreases the time until the next slip event.

For earthquakes, the analogy implies that earthquake occurrence on a segment of a fault may reflect changes in the stress on the fault resulting from earthquakes elsewhere. This concept is quantified using the Coulomb–Mohr criterion (Eqn 5) that sliding can occur when the shear stress exceeds that on the sliding line (Fig. 5.7-9), or  $\tau > \mu\sigma$ . We can thus define the Coulomb failure stress

$$\sigma_f = \tau + \mu\sigma \quad (55)$$

such that failure occurs when  $\sigma_f$  is greater than zero. Whether a nearby earthquake brings a fault closer to or further from failure is shown by the change in Coulomb failure stress due to the earthquake,

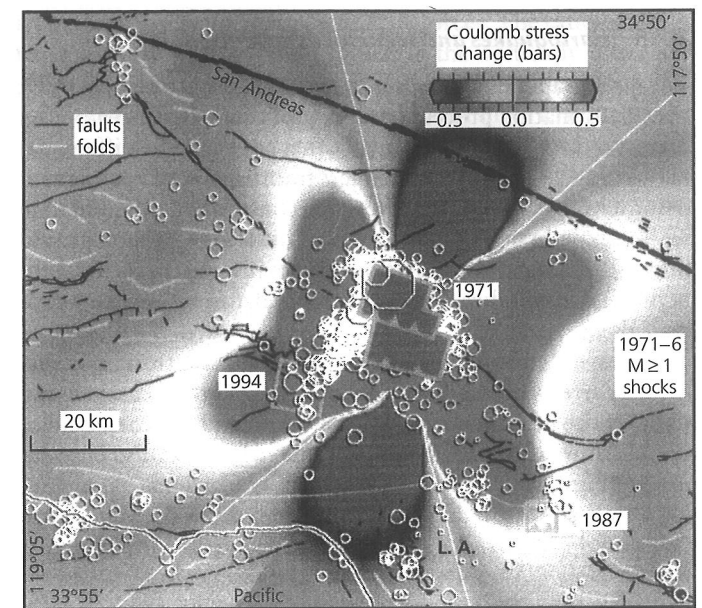


Fig. 5.7-25 Predicted changes in Coulomb failure stress due to the 1971 San Fernando earthquake. The Whittier Narrows and Northridge earthquakes subsequently occurred in regions where the 1971 earthquake increased the failure stress. (Stein *et al.*, 1994. *Science*, 265, 1432–5, copyright 1994 American Association for the Advancement of Science.)

$$\Delta\sigma_f = \Delta\tau + \mu\Delta\sigma. \quad (56)$$

Failure is favored by positive  $\Delta\sigma_f$ , which can occur either from increased shear stress  $\tau$  or a reduced normal stress (compression is negative, so  $\Delta\sigma > 0$  favors sliding).

Some earthquake observations provide support for this idea. Figure 5.7-25 shows the predicted Coulomb failure stress changes in the Los Angeles region due to the 1971 ( $M_s 6.6$ ) San Fernando earthquake. The stress change pattern reflects the earthquake's focal mechanism, thrust faulting on a NW–SE-striking fault (Fig. 5.2-3). Two moderate earthquakes, the 1987 Whittier Narrows ( $M_L 5.9$ ) and 1994 Northridge ( $M_w 6.7$ ) earthquakes subsequently occurred in regions where the 1971 earthquake increased the failure stress, suggesting that the stress change may have had a role in triggering the earthquakes. A similar pattern has been found after other earthquakes, and some studies have found that aftershocks are concentrated in regions where the mainshock increased the failure stress. Stress triggering may explain why successive earthquakes on a fault sometimes seem to have a coherent pattern. For example, the 1999  $M_s 7.4$  Izmit earthquake on the North Anatolian fault (Fig. 5.6-8) appears to be part of a sequence of major ( $M_s 7$ ) earthquakes over the past 60 years, which occurred successively further to the west, and hence closer to the metropolis of Istanbul.

An intriguing feature of such models is that the predicted stress changes are of the order of 1 bar, or only 1–10% of the typical stress drops in earthquakes (Section 4.6.3). Such small

stress changes should only trigger an earthquake if the tectonic stress is already close to failure. However, as in the slider model (Fig. 5.7-24), stress changes can affect the time until the tectonic stress is large enough to produce earthquakes. It has been argued that the 1906 San Francisco earthquake reduced the failure stress on other faults in the area, causing a "stress shadow" and increasing the expected time until the next earthquake on these faults. This is consistent with the observation that during the 75 years before the 1906 earthquake, the area had 14 earthquakes with  $M_w$  above 6, whereas only one occurred in the subsequent 75 years. Such analyses may help improve estimates of the probability that an earthquake of a certain size will occur on a given fault during some time period. To date, such estimates have large uncertainties (Section 4.7.3), in part because of the large variation in the time intervals between earthquakes. Stress loading models, some of which incorporate rate- and state-dependent friction because simple Coulomb friction does not predict large enough changes in recurrence time, may explain some of the variations and thus reduce these uncertainties.

This discussion brings out the importance of understanding the state of stress on faults. On this issue, the friction models give some insight, but major questions remain. Earthquake stress drops estimated from seismological observations are typically less than a few hundred bars (tens of MPa). Yet, the expected strength of the lithosphere (e.g., Fig. 5.7-14–16) is much higher, in the kilobar (hundreds of MPa) range. The laboratory results (Fig. 5.7-20) and frictional models (Fig. 5.7-21) suggest an explanation for this difference, because in both the stress drop during a slip event is only a fraction of the total stress.

However, the frictional models do not explain an intriguing problem called the "San Andreas" or "fault strength" paradox. As noted in Section 5.4.1, a fault under shear stress  $\tau$  slipping at rate  $v$  should generate frictional heat at a rate equal to  $\tau v$ . Thus, if the shear stresses on faults are as high (kbar or hundreds of MPa) as expected from the strength envelopes, significant heat should be produced. But little if any heat flow anomaly is found across the San Andreas fault (Fig. 5.7-26), suggesting that the fault is much weaker than expected. A similar conclusion emerges from consideration of stress orientation data. Although the Coulomb–Mohr model predicts that the maximum principal stress directions inferred from focal mechanisms, geological data, and boreholes should be about  $23^\circ$  from the San Andreas fault (Fig. 5.7-8), the observed directions are essentially perpendicular to the fault (Fig. 5.6-19), implying that the fault acts almost like a free surface. To date, there is no generally accepted explanation for these observations. The most obvious one is that the effective stress on the fault is reduced by high pore pressure, but there is discussion about whether pressures much higher than hydrostatic pressure could be maintained in the fault zone. An alternative explanation, that the fault zone is filled by low-strength clay-rich fault gouge, faces the difficulty that experiments on such material find that it has normal strength unless pore pressures are high.

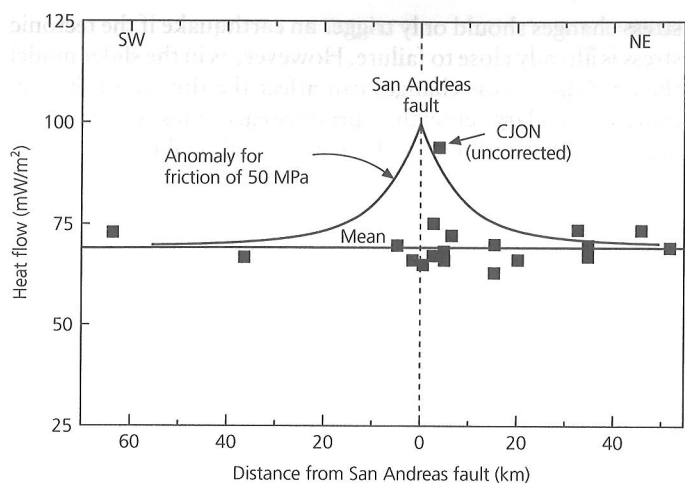


Fig. 5.7-26 Observed (squares) heat flow across the San Andreas fault. The elevated heat flow predicted by shear heating (solid line) is not observed, except for one point (CJON, Cajon pass), where alternative interpretations are possible, implying that the fault is weak. (Lachenbruch and Sass, 1988. *Geophys. Res. Lett.*, 15, 981–4, copyright by the American Geophysical Union.)

In summary, ideas based on rock friction are providing important insights into earthquake mechanics. Although many issues remain unresolved, and some attractive notions remain to be fully demonstrated, rock friction seems likely to play a growing role in addressing earthquake issues.

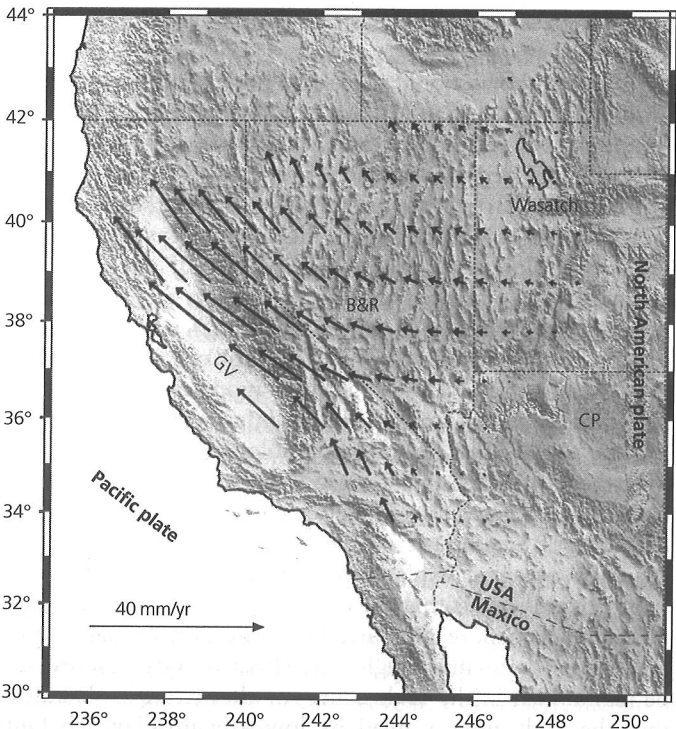


Fig. 5.7-27 Left: Estimated velocity field for part of the Pacific–North America plate boundary zone in the western USA. Right: Effective viscosity determined by dividing the magnitude of the deviatoric stress tensor by the magnitude of the strain rate tensor. (Flesch et al., 2000. *Science*, 287, 834–6, copyright 2000 American Association for the Advancement of Science.)

### 5.7.6 Earthquakes and regional deformation

The large, rapid deformation in earthquakes is often part of a slow deformation process occurring over a broader region. As discussed in Section 5.6.2, there often appear to be differences between the seismic, aseismic, transient, and permanent deformations sampled by different techniques on different time scales. Experimental and theoretical ideas about rheology and lithospheric dynamics are being used to investigate the relation between earthquakes and the regional deformations that produce them.

We have seen that earthquakes often reflect deformation distributed over a broad plate boundary zone. In this case, we can think of the lithosphere as a viscous fluid and use earthquakes as indicators of its deformation. This idea is like the physical model (Fig. 5.6-7) that used deformable plasticine as an analogy for the deformation of Asia resulting from the Himalayan collision. Figure 5.7-27 shows such an analysis for part of the Pacific–North America plate boundary zone in the western United States. The deformation is assumed to result from a combination of forces due to the transform plate boundary and forces due to the potential energy of elevated topography, which tends to spread under its own weight. To test this idea, a continuous velocity field has been interpolated from space-geodetic, fault slip, and plate motion data (Figs 5.2-3 and 5.6-3). The velocity field is treated as being due to the motion of a viscous fluid, and is converted to a strain rate tensor field. This is then compared to the magnitude of the stress tensor inferred

from topography and plate boundary forces. The ratio of stress to strain rate at any point, which is the vertically averaged effective viscosity, varies significantly. Low values along the San Andreas fault and western Great Basin show that the strain rates are relatively high for the predicted stress, consistent with a weak lower crust. The Great Valley–Sierra Nevada block has little internal deformation, and thus acts relatively rigidly and appears as a high-viscosity region. Summing seismic moment tensors (Section 5.6.2) yields a seismic strain rate averaging about 60% of the inferred total strain. As discussed earlier, this discrepancy may indicate some aseismic deformation or that the 150 years of historical seismicity is too short for a reliable estimate.

Viscous fluid models can be used to study how the lithosphere deforms on different time scales. For example, as noted in Section 5.6.2, GPS data across the entire Nazca–South America plate boundary zone show faster motion than is inferred from structural geology or topographic modeling. The difference probably occurs because the GPS data record instantaneous velocities that include both permanent deformation and elastic deformation that will be recovered during future earthquakes, whereas the lower geological rates reflect only the permanent deformation. This can be modeled by representing the overriding South American plate using a simple one-dimensional system of a spring, a dashpot, and a pair of frictional plates (Fig. 5.7-28). This system approximates the behavior of the crust: the spring gives the elastic response over short periods, the dashpot gives the viscous response over geological time scales, and the frictional plates simulate the thrust faulting earthquake cycle at the trench. As plate convergence compresses the system, the stress  $\sigma(t)$  increases with time until it reaches a yield strength  $\sigma_y$ , when an earthquake occurs, stress drops to  $\sigma_b$ , and the process repeats. Displacement accumulates at a rate  $v_0$  except during earthquakes, when the displacement drops by an amount  $\Delta u$ . The topography and geologic data record the averaged long-term shortening rate  $v_c$  shown by the envelope of the sawtooth curve, whereas GPS data record the higher instantaneous velocity  $v_0$ . The instantaneous velocity thus results from the portion of the plate motion locked at the trench that deforms the overriding plate elastically (Fig. 4.5-14) and is released as seismic slip in interplate earthquakes. By contrast, the aseismic slip component at the trench has no effect because it does not contribute to locking on the interface and deformation of the overriding plate. Similar models are being explored for other regions where deformation appears to vary on different time scales.

Viscous fluid models are also used to analyze other aspects of the earthquake cycle. For example, Fig. 5.7-29 shows the strain rate near portions of the San Andreas fault compared to the time since the last great earthquake on that portion of the fault. Postseismic motion seems to continue for a period of years after an earthquake and then slowly decays, presumably due to the steady interseismic motion. A similar picture emerges from GPS and other geodetic results following large trench thrust faulting earthquakes. For a number of years, sites near the trench on the overriding plate move seaward, showing

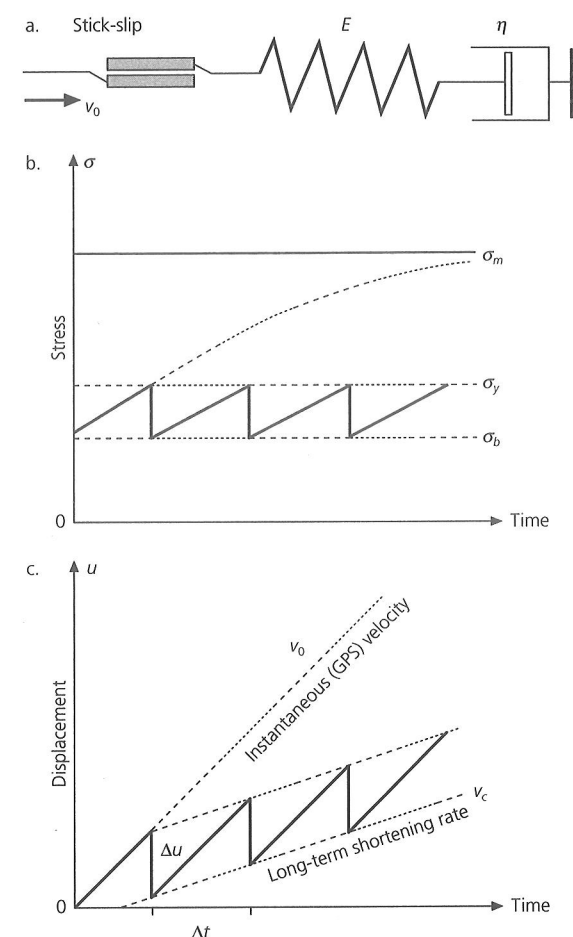


Fig. 5.7-28 a: Model for a viscoelastic–plastic crust to describe the response of the overriding South American plate to the subduction of the Nazca plate. The dashpot represents a viscous body modeling the permanent deformation, the spring represents an elastic body modeling the transient deformation, and the frictional plates represent the earthquake cycle at the trench. b: Stress evolution for the model. c: Displacement history for the model. Displacement accumulates at the instantaneous rate  $v_0$  except during earthquakes, when slip  $\Delta u$  occurs. GPS data record a gradient starting at  $v_0$  from the trench, whereas the envelope of the displacement curve  $v_c$  is the long-term shortening rate reflected in geological records and topography. (Liu et al., 2000. *Geophys. Res. Lett.*, 28, 3005–8, copyright by the American Geophysical Union.)

postseismic motion consistent with the earthquake focal mechanism (Fig. 4.5-15). Eventually, however, the sites resume the landward interseismic motion usually seen at trenches (Fig. 5.6-10). Such observations are challenging to interpret, because postseismic afterslip on or near a fault can have effects at the surface similar to viscoelastic flow of the asthenosphere (Fig. 5.7-29), but offer the prospect of improving our understanding of both earthquake processes and the rheology of the lithosphere and the asthenosphere. A tantalizing possibility is that the viscous asthenosphere permits stress waves generated by large earthquakes to travel slowly for large distances and contribute to earthquake triggering.

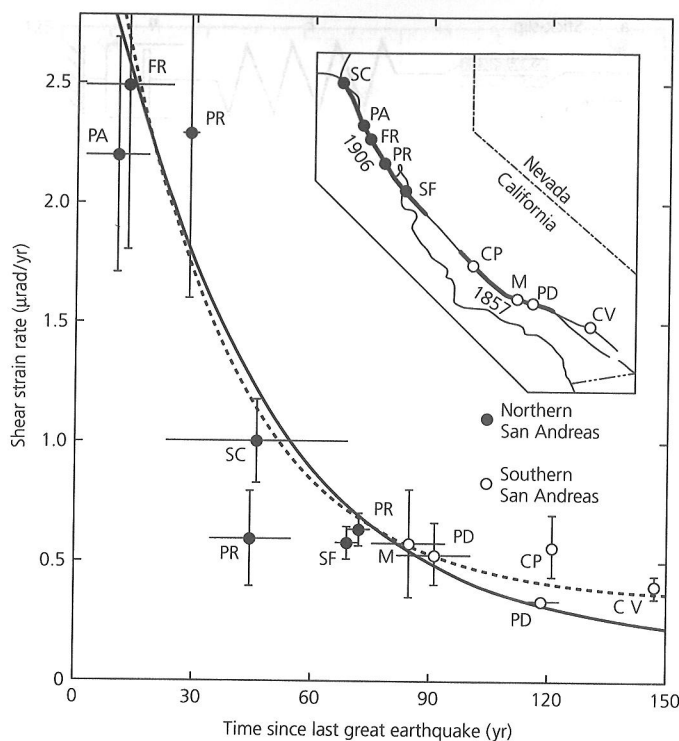


Fig. 5.7-29 Shear strain rate near portions of the San Andreas fault compared to the time since the last great earthquake. The data are similar to the predictions of two alternative models: viscoelastic stress relaxation (solid curve) and aseismic postseismic slip beneath the earthquake fault plane (dashed line). (Thatcher, 1983. *J. Geophys. Res.*, 88, 5893–902, copyright by the American Geophysical Union.)

## Further reading

Given the comparatively recent discovery of plate tectonics, its importance for most aspects of geology, and its crucial role in the earthquake process, many excellent sources, a few of which are listed here, offer more information about this chapter's topics.

The dramatic development of plate tectonics is discussed from the view of participants by Menard (1986) and in Cox's (1973) collection of classic papers. Basic ideas in plate tectonics are treated in most introductory and structural geology texts. More detailed treatments include Uyeda (1978), Fowler (1990), Kearny and Vine (1990), and Moores and Twiss (1995). Cox and Hart (1986) present the basic kinematic concepts, and global

plate motion models are discussed by Chase (1978), Minster and Jordan (1978), and DeMets *et al.* (1990).

Thermal and mechanical aspects of plate tectonics are discussed by Turcotte and Schubert (1982) and Sleep and Fujita (1997). Mid-ocean ridge tectonics and structure are discussed by Solomon and Toomey (1992) and Nicolas (1995). The thermal evolution of oceanic lithosphere is discussed by Parsons and Sclater (1977) and Stein and Stein (1992); McKenzie (1969) presents the subduction zone thermal model we follow. Papers in Bebout *et al.* (1996) cover many aspects of subduction, and Kanamori (1986) reviews subduction zone thrust earthquakes. Lay (1994) treats the nature and fate of subducting slabs, and deep earthquakes are reviewed by Frohlich (1989), Green and Houston (1995), and Kirby *et al.* (1996b). For a derivation of the ridge push force see Parsons and Richter (1980); Wiens and Stein (1985) discuss its application to oceanic intraplate stresses. Yeats *et al.* (1997) cover a wide variety of topics about the relation of earthquakes to regional geology. Rosendahl (1987) reviews continental rifting. Papers in Gregersen and Basham (1989) treat aspects of passive margin and continental interior earthquakes with emphasis on postglacial effects.

Concepts in continental deformation are treated by Molnar (1988) and England and Jackson (1989); Gordon (1998) gives an overview of plate rigidity and diffuse plate boundaries. Applications of space geodesy to tectonics are reviewed by papers in Smith and Turcotte (1993) and by Dixon (1991), Gordon and Stein (1992), and Segall and Davis (1997). Many GPS data and results, including an overview brochure, can be found on the University NAVSTAR Consortium WWW site <http://www.unavco.org>. Stress maps and their interpretations are discussed by Zoback (1992) and other papers in the same journal issue; stress maps are available at the World Stress Map project WWW site <http://www-wsm.physik.uni-karlsruhe.de>.

Mantle plumes in general are reviewed by Sleep (1992); Nataf (2000) and Foulger *et al.* (2001) discuss seismic imaging of plumes; Smith and Braile (1994) discuss the Yellowstone hot spot; and Stein and Stein (1993) discuss oceanic hot spot swells. Papers in Peltier (1989) treat many aspects of mantle convection; Silver *et al.* (1988) explore the relationship between subduction, convection, and mantle structure; and Christensen (1995) reviews the effects of phase transitions on mantle convection. The heat engine perspective on global tectonics is discussed by Stacey (1992), and Ward and Brownlee (2000) summarize the arguments advocating a crucial role for plate tectonics in the origin and survival of life on Earth.

Topics involving rock mechanics, flow, and their tectonic applications are discussed by Jaeger (1970), Weertman and Weertman (1975), Jaeger and Cook (1976), Turcotte and Schubert (1982), Kirby (1983), Kirby and Kronenberg (1987), and Ranalli (1987). Scholz (1990) and Marone (1998) cover topics dealing with the relation of rock mechanics to earthquakes, with special emphasis on rock friction. Our treatment of the slider model for faulting follows Scholz (1990). Related topics, including issues of continental deformation and fault strength, are also treated by papers in Evans and Wong (1992). Stein (1999) summarizes the concept of stress triggering of earthquakes.